

ARTICLE

Upregulation of VCAM-1 in lymphatic collectors supports dendritic cell entry and rapid migration to lymph nodes in inflammation

Jorge Arasa^{1*}, Victor Collado-Diaz^{1*}, Ioannis Kritikos¹, Jessica Danielly Medina-Sanchez¹, Mona Carina Friess¹, Elena Caroline Sigmund¹, Philipp Schineis¹, Morgan Campbell Hunter¹, Carlotta Tacconi¹, Neil Paterson^{2,3,4}, Takashi Nagasawa⁵, Friedemann Kiefer^{6,7}, Tajia Makinen⁸, Michael Detmar¹, Markus Moser^{9,10}, Tim Lämmermann², and Cornelia Halin¹

Dendritic cell (DC) migration to draining lymph nodes (dLNs) is a slow process that is believed to begin with DCs approaching and entering into afferent lymphatic capillaries. From capillaries, DCs slowly crawl into lymphatic collectors, where lymph flow induced by collector contraction supports DC detachment and thereafter rapid, passive transport to dLNs. Performing a transcriptomics analysis of dermal endothelial cells, we found that inflammation induces the degradation of the basement membrane (BM) surrounding lymphatic collectors and preferential up-regulation of the DC trafficking molecule VCAM-1 in collectors. In crawl-in experiments performed in ear skin explants, DCs entered collectors in a CCR7- and $\beta 1$ integrin-dependent manner. In vivo, loss of $\beta 1$ -integrins in DCs or of VCAM-1 in lymphatic collectors had the greatest impact on DC migration to dLNs at early time points when migration kinetics favor the accumulation of rapidly migrating collector DCs rather than slower capillary DCs. Taken together, our findings identify collector entry as a critical mechanism enabling rapid DC migration to dLNs in inflammation.

Introduction

Afferent lymphatic vessels mediate the transport of antigen and the migration of leukocytes from peripheral tissues to draining LNs (dLNs) and are important for the induction and regulation of immune responses (Schineis et al., 2019; Worbs et al., 2017). They originate in the tissue as blind-ended lymphatic capillaries that feed into collecting vessel segments. The latter merge into larger collectors, which exit the tissue and connect with dLNs. While capillaries are the site of fluid uptake, collectors are specialized in fluid transport. Lymphatic endothelial cells (LECs) in capillaries have an oak-leaf shape and are connected by button-like cell-cell junctions (Baluk et al., 2007). This setup gives rise to characteristic flaps, so-called primary valves, which facilitate the uptake of lymph components, i.e., of tissue fluids, (macro)molecules, and cells (Baluk et al., 2007; Pflücke and Sixt, 2009). Capillaries typically have a wide lumen and are surrounded by a very thin and highly fenestrated basement membrane (BM). By contrast, LECs in the fluid-tight collectors

display an elongated shape and are connected by continuous zipper-like cell-cell junctions. Collectors are also surrounded by a thicker BM and are covered by contracting lymphatic muscle cells (LMCs). Moreover, they contain valves to further facilitate fluid propagation (Moore and Bertram, 2018).

The best-studied leukocyte cell type migrating via afferent lymphatics are dendritic cells (DCs; Worbs et al., 2017). DC migration constantly occurs under steady-state conditions, but it is strongly increased under inflammatory conditions (Ohl et al., 2004; Vigl et al., 2011). Migration is highly dependent on the lymphatic-expressed chemokine CCL21 (Ohl et al., 2004; Vigl et al., 2011; Weber et al., 2013), which is the ligand of CCR7, a chemokine receptor up-regulated on maturing DCs (Förster et al., 1999). In steady-state, DC migration to dLNs was shown to be integrin independent (Lämmermann et al., 2008), whereas under inflammatory conditions, when LECs up-regulate the integrin ligands ICAM-1 and vascular cell adhesion molecule-

¹Institute of Pharmaceutical Sciences, ETH Zurich, Zurich, Switzerland; ²Max Planck Institute of Immunobiology and Epigenetics, Freiburg, Germany; ³Faculty of Biology, University of Freiburg, Freiburg, Germany; ⁴International Max Planck Research School for Immunobiology, Epigenetics and Metabolism, Freiburg, Germany; ⁵Laboratory of Stem Cell Biology and Developmental Immunology, Graduate School of Frontier Biosciences and Graduate School of Medicine, Osaka University, Osaka, Japan; ⁶Max Planck Institute for Molecular Biomedicine, Münster, Germany; ⁷European Institute for Molecular Imaging, Westfälische Wilhelms-Universität Münster, Münster, Germany; ⁸Department of Immunology, Genetics and Pathology, Uppsala University, Uppsala, Sweden; ⁹Max Planck Institute of Biochemistry, Martinsried, Germany; ¹⁰Institute of Experimental Hematology, Technical University Munich, Munich, Germany.

*J. Arasa and V. Collado-Diaz contributed equally to this paper; Correspondence to Cornelia Halin: cornelia.halin@pharma.ethz.ch.

© 2021 Arasa et al. This article is distributed under the terms of an Attribution–Noncommercial–Share Alike–No Mirror Sites license for the first six months after the publication date (see <http://www.rupress.org/terms/>). After six months it is available under a Creative Commons License (Attribution–Noncommercial–Share Alike 4.0 International license, as described at <https://creativecommons.org/licenses/by-nc-sa/4.0/>).

1 (VCAM-1), DC and T cell migration becomes integrin dependent (Johnson et al., 2006; Teijeira et al., 2013; Teijeira et al., 2017). Even though DC migration to dLNs is enhanced under inflammatory conditions, it generally remains a fairly slow process. While arrival of dermal DCs reportedly peaks 1–2 d after exposure to a migration-inducing stimulus, epidermal Langerhans cells only reach maximal numbers in dLNs after 3–4 d (Kissenpfennig et al., 2005; Tomura et al., 2014). The slow kinetics can be attributed to the fact that before migration, DCs first need to mature and up-regulate CCR7. Additionally, a large part of the DCs' displacement from skin to dLNs requires active cell migration, which per se is a rather slow process. Early studies based on electron and confocal microscopy (Baluk et al., 2007) and time-lapse imaging (Pflücke and Sixt, 2009) have established that DCs and other leukocytes approach and enter afferent lymphatic vessels at the level of the lymphatic capillaries, by squeezing through the characteristic open flaps. Intravital microscopy (IVM) studies have subsequently shown that DCs and T cells need to actively crawl in the capillary lumen (Nitschké et al., 2012; Schineis et al., 2019; Tal et al., 2011), since the lymph flow in this compartment is too low (Berk et al., 1996; Swartz et al., 1996) to support passive transport. Rather than migrating straight toward the downstream collectors, DCs frequently arrest and patrol within capillaries (Hunter et al., 2019; Nitschké et al., 2012). We previously found that this mode of migration is semi-directed and that only ~20% of the DC's net movement (corresponding to ~1.2 $\mu\text{m}/\text{min}$) advances the cell in the downstream direction of the dLN (Russo et al., 2016). Transition to a much more rapid form of transport occurs in contracting collecting vessels once hydrodynamic forces increase. Now leukocytes start to detach and are rapidly transported by the lymph flow to the dLN, at velocities ranging from ~1 mm/min in small dermal collectors (Teijeira et al., 2017) to several millimeters per second in large collecting vessels (Akl et al., 2011; Dixon et al., 2006). This impressive acceleration by several log units illustrates that, even once a DC has entered into lymphatics, the many hours spent in lymphatic capillaries remain rate-limiting in the DC's propagation to a dLN. Currently, it is not known whether, in addition to flow, gene expression differences between LECs in lymphatic capillaries and in collectors (capLECs and colLECs, respectively) contribute to the distinct migration pattern observed in these two vascular beds.

In this study, we performed a transcriptomics analysis of capLECs and colLECs isolated from uninflamed and inflamed murine ear skin in order to identify new mediators or pathways involved in leukocyte trafficking. Unexpectedly, we found VCAM-1 and other molecules involved in inflammation-induced DC migration as well as proteins mediating extracellular matrix (ECM) remodeling to be preferentially up-regulated in inflamed dermal colLECs over capLECs. This prompted us to investigate whether in inflammation DCs might enter lymphatics not only via capillaries but additionally via collectors. Performing time-lapse imaging, DC crawl-in studies in skin explants, and in vivo migration studies, we here show that preferential up-regulation of VCAM-1 in inflamed collectors opens up a new, integrin β 1-mediated route for DC entry into dermal collectors. Our data further indicate that—by bypassing the slow, active migration

step in lymphatic capillaries—integrin β 1/VCAM-1-controlled entry into contracting collectors generates a shortcut for rapid DC migration to dLNs.

Results

Lymphatic capillaries and collectors are present in murine and human skin and can be distinguished by LYVE-1 expression

In response to tissue inflammation, dermal LECs up-regulate various adhesion molecules and chemokines, which reportedly contribute to increasing DC migration (Johnson et al., 2006; Johnson and Jackson, 2013; Martín-Fontecha et al., 2003; Vigl et al., 2011). However, the exact anatomical location in the lymphatic vessel tree where this up-regulation occurs is presently unknown. Considering that dermal lymphatics can be subdivided into initial capillaries and downstream collectors (Schineis et al., 2019; Ulvmar and Mäkinen, 2016), we wanted to study inflammation-induced gene expression changes in capLECs and colLECs, respectively. To distinguish capLECs from colLECs, we used the marker LYVE-1, which is expressed in dermal lymphatic capillaries but not in collecting vessels (Fig. 1 A; Mäkinen et al., 2005; Wang et al., 2014). We confirmed the suitability of LYVE-1 to accurately distinguish dermal capLECs from colLECs by staining murine ear skin whole-mounts with the lymphatic marker PROX1 and costaining with LYVE-1 and the junctional protein vascular endothelial (VE)-cadherin. VE-cadherin displayed a button-like expression in LYVE-1⁺ capillaries, around the characteristic open flaps, and a zipper-like expression in LYVE-1⁻ collecting vessel segments (Fig. S1, A and B; Baluk et al., 2007). Moreover, the collector-marker α smooth muscle actin (α SMA) as well as the BM component laminin were significantly reduced in LYVE-1⁺ vessels (Fig. S1, C–F; Pflücke and Sixt, 2009; Ulvmar and Mäkinen, 2016). Similar to murine skin (Fig. 1 A), LYVE-1⁻ podoplanin⁺ α SMA⁺ collecting vessels were identified in deeper regions of the human dermis, demonstrating that both capillaries and collectors are also present in human skin (Fig. S1, G and H).

Transcriptional analysis of capLECs, colLECs, and blood vascular endothelial cells (BECs) isolated from inflamed and uninflamed mouse skin

To study inflammation-induced changes in all endothelial cells, we elicited a contact hypersensitivity (CHS) response to 4-ethoxymethylene-2-phenyl-2-oxazoline-5-1 (oxazolone) in the ear skin of mice and isolated capLECs (CD45⁻ CD31⁺ podoplanin⁺ LYVE-1⁺), colLECs (CD45⁻ CD31⁺ podoplanin⁺ LYVE-1⁻), and BECs (CD45⁻ CD31⁺ podoplanin⁻ LYVE-1⁻) by FACS sorting from tissue single-cell suspensions (Fig. S2 A). RNA extracted from endothelial cells was converted into cDNA and analyzed by RNA sequencing. Among 22,880 annotated genes, 2,131 were found to be differentially expressed in steady-state and 2,070 in inflammation in the three different cell populations (cutoff of 0.5-fold for gene expression and P value <0.05; Fig. S2, B and C). Principal component analysis revealed six clearly distinguishable gene-expression signatures corresponding to steady-state control (CTR) and CHS-inflamed (CHS-INF) capLECs, colLECs, and BECs, respectively (Fig. 1 B). These findings were further

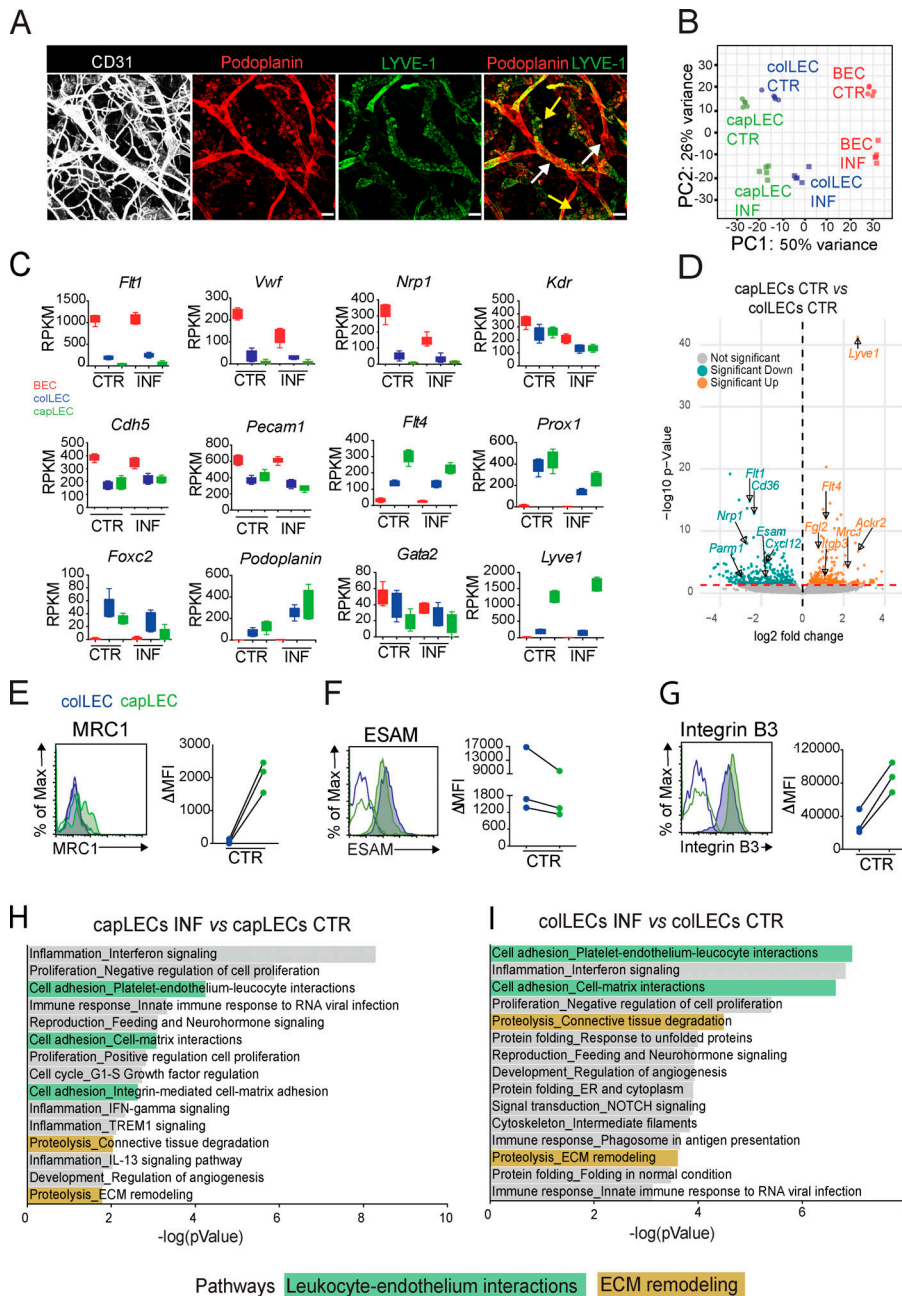


Figure 1. RNA sequencing of LECs derived from lymphatic capillaries and collectors and BECs isolated from murine skin. (A) Representative whole-mount images of steady-state mouse ear skin showing dermal blood vessels (CD31⁺podoplanin⁻), lymphatic collectors (CD31⁺podoplanin⁺LYVE-1⁻; white arrows) and lymphatic capillaries (CD31⁺podoplanin⁺LYVE-1⁺; yellow arrows). Scale bar, 50 μm. (B) Principal component analysis of capLECs, colLECs, and BECs from CTR and INF conditions (n = 5 experimental replicates). (C) Reads per kilobase per million mapped reads (RPKM) plots of vascular marker genes. Box shows median, 25%, and 75% percentile; whiskers show minimum and maximum. (D) Volcano plot of capLECs versus colLECs in steady-state (CTR) conditions (0.5-fold change; P value, 0.05). (E–G) FACS was performed on CTR skin single-cell suspensions following the gating scheme in Fig. S2 A. Analysis of MRC1 (E), ESAM (F), and ITGB3 (G). Representative FACS plots and ΔMFI of three independent experiments are shown. (H and I) Identification of specific differentially regulated pathways in CTR versus INF capLECs (H) and colLECs (I). MetaCore Process network 1.5-fold change; P value, 0.05; deregulated pathways. Max, maximum; MFI, median fluorescent intensity.

supported by the hierarchical clustering of the different datasets (Fig. S2 D). The normalized expression of vascular marker genes exhibited the expected signatures for BEC markers like VEGFR1 (*Flt1*), von Willebrand factor (*Vwf*), or neuropilin 1 (*Nrp1*); pan-endothelial markers like VEGFR2 (*Kdr*), VE-cadherin (*Cdh5*), and CD31 (*Pecam1*); and LEC markers like *Flt4* (VEGFR3) and *Prox1* (Fig. 1 C and Fig. S2 E). As expected, *Foxc2* and *Gata2*, which are involved in lymphatic valve development and maintenance (Ulvmar and Mäkinen, 2016), were more highly expressed in colLECs than in capLECs (Fig. 1 C). Consistent with our sorting strategy, both colLECs and capLECs abundantly expressed *Podoplanin*, while only capLECs had high *Lyve1* transcript levels (Fig. 1 C). In agreement with the gene expression differences observed between CTR capLECs and colLECs (Fig. 1 D), differential protein expression could be confirmed by FACS analysis

for MRC1, the endothelial cell adhesion molecule (ESAM), and ITGB3 (Fig. 1, E–G).

Pathways related to leukocyte-endothelium interactions and ECM remodeling are enriched in capLECs and colLECs during inflammation

We next enriched for the most deregulated pathways by performing MetaCore Process Network analysis (cutoff of 1.5-fold change in gene expression and P value <0.05). As expected, several pathways related to inflammation or proliferation were deregulated in both capLECs and colLECs during the inflammatory response (Fig. 1, H and I). However, somewhat surprisingly, not only capLECs but also colLECs displayed enrichment of pathways related to leukocyte-endothelium interactions and ECM remodeling in inflammation (Fig. 1 I). This suggested that

inflamed lymphatic collectors might not only serve in the propagation of leukocytes by flow but also actively participate in immune cell entry.

CXCL12, CX3CL1, and VCAM-1 are up-regulated in inflamed collectors

When investigating the expression profiles of adhesion molecules and chemokines, we found that these were generally up-regulated in both capLECs and colLECs during CHS-induced inflammation (Fig. 2 A). Selectins were more up-regulated in colLECs, whereas *Icam1* and inflammatory chemokines like *Cxcl9*, *Cxcl10*, or *Ccl2* were up-regulated in both capLECs and colLECs. Surprisingly, the chemokines *Cx3cl1* and *Cxcl2* and the adhesion molecule *Vcam1*, which have all been previously shown to mediate DC migration in inflammation (Johnson et al., 2006; Johnson and Jackson, 2013; Kabashima et al., 2007; Teoh et al., 2009), were preferentially up-regulated or expressed in colLECs (Fig. 2, A and B). In line with the transcriptomic data, whole-mount immunofluorescence performed in CTR and INF ear skin revealed CX3CL1 protein expression in inflamed collectors but much less in capillaries (Fig. 2 C). Ear skin whole-mounts of *Cxcl2-GFP* reporter mice (Ara et al., 2003) detected only faint GFP signals in LECs but a strong signal in collector-surrounding accessory cells, which likely were LMCs (Fig. 2 D). Similarly, in whole-mount analyses, VCAM-1 was expressed in some uninfamed collectors and up-regulated in inflamed collectors (Fig. 2 E). Preferential expression and up-regulation of VCAM-1 in colLECs as compared with capLECs was also confirmed by FACS performed on CTR and INF ear skin (Fig. 2, F-I). Surprisingly, the chemokine *Ccl2l*, the most important chemokine driving DC migration to dLNs, was not detected in our sequencing data. However, performing whole-mount histology, we could identify characteristic intracellular CCL21 deposits as well as extracellular CCL21 in and around both lymphatic capillaries and collectors (Fig. S3 A), as previously reported (Reynolds et al., 2021; Russo et al., 2016). In addition, performing quantitative PCR on sorted LECs, we found *Ccl2l* to be more highly expressed in capLECs than in colLECs (Fig. S3 B).

DCs enter into collectors in a CCR7-dependent manner

Given the expression of well-known DC trafficking molecules in collectors (Fig. 2; and Fig. S3, A and B), we next investigated whether bone marrow-derived DCs might not only enter into capillaries, as generally assumed (Pflücke and Sixt, 2009), but directly into collectors. To this end, we performed DC crawl-in studies in dorsal ear skin explants, which in contrast to the ventral ear aspects contain a high proportion of lymphatic collectors in the central region (Fig. 3, A and B). Notably, we observed that in this assay, the mere ripping of ear skin along the cartilage, to expose the dermal aspects before adding the DCs, induced a strong inflammatory response, as evidenced by a general up-regulation of lymphatic ICAM-1 4 h after ripping (Fig. S3, C-E). In agreement with our findings in the CHS model (Fig. 2, E-I), we also observed preferential up-regulation of VCAM-1 in colLECs as compared with capLECs at this time point (Fig. S3, F-K). To investigate whether DCs enter into dermal collectors, we performed crawl-in assays in dorsal explants

prestained with fluorophore-coupled anti-CD31 and anti-LYVE-1 antibodies before adding YFP⁺ bone marrow-derived DCs (Lindquist et al., 2004). After 30 min, most DCs colocalized with lymphatic capillaries and collectors (Fig. 3 C). In capillaries, many DCs with a clear intraluminal localization were detectable after 30–45 min of incubation (Fig. 3, C and D), in agreement with previous reports (Lämmermann et al., 2008; Pflücke and Sixt, 2009). Conversely, DCs took 2–4 h to enter into collectors (Fig. 3 D). Notably, many DCs observed within LYVE-1⁻ collectors after 2–4 h were at a considerable distance (>250 μm) from LYVE-1⁺ capillaries (Fig. 2 C). This made it highly unlikely that those cells had arrived in collectors indirectly, i.e., after initial entry into capillaries followed by intralymphatic crawling, which reportedly would only advance them with a velocity of ~1.2 μm/min in the direction of the collectors (Russo et al., 2016). To directly address the entry question, we performed time-lapse imaging in dorsal ear skin explants. This allowed us to capture DCs entering into capillaries (Video 1), but also into vessels with collector-like morphology (Video 2) and into vessels unambiguously identified as collectors by the absence of LYVE-1 expression (Video 3). We could also confirm this observation by IVM, showing a DC entering into a contracting lymphatic collector in inflamed ear skin (Video 4). To investigate the CCR7 dependence of DC entry into collectors, we performed competitive crawl-in experiments by coincubating ear skin explants with 1:1 ratios of differentially labeled WT and *Ccr7*^{-/-} DCs. When analyzing the explants 4 h later, we found that in both vessel segments, WT DCs clearly outnumbered the *Ccr7*^{-/-} DCs (Fig. 3, E and F). Thus, in agreement with CCL21's expression in both capillaries and collectors (Fig. S3, A and B), our data demonstrated the CCR7 dependence of DC entry into both vessel segments.

DC entry into lymphatic collectors is talin1 and integrin β1 dependent

We next focused on VCAM-1, a well-described DC trafficking molecule (Johnson et al., 2006; Teoh et al., 2009). The VCAM-1 ligand expressed on DCs is the integrin VLA-4, which comprises an α4 and a β1 subunit (Nourshargh et al., 2010). To investigate the requirement for integrins, and specifically for α4β1, in DC entry into lymphatic collectors, we generated bone marrow-derived DCs deficient in either integrin β1 or talin1, an intracellular adaptor essential for all integrin-mediated migration steps (Calderwood and Ginsberg, 2003). We next performed competitive crawl-in experiments by adding 1:1 ratios of WT and either talin1-deficient (*Tln1*^{-/-}) or integrin β1-deficient (*Itgbl1*^{-/-}) DCs to the ear skin explants. When quantifying DCs within lymphatics 4 h after starting the crawl-in assays, we found that the ratio of *Tln1*^{-/-}:WT DCs was reduced in both capillaries and collectors (Fig. 3, G and H), likely as a consequence of ICAM-1 up-regulation by both dermal capLECs and colLECs (Fig. S3, D and E). When performing crawl-in experiments with *Itgbl1*^{-/-} DCs, we found that the ratio of *Itgbl1*^{-/-}:WT DCs was unchanged in capillaries, but was significantly reduced in collectors (Fig. 3, I and J), i.e., in the vascular bed in which we had observed preferential VCAM-1 up-regulation (Fig. S3, F-K). Since we frequently observed *Itgbl1*^{-/-} DCs accumulating outside of collectors

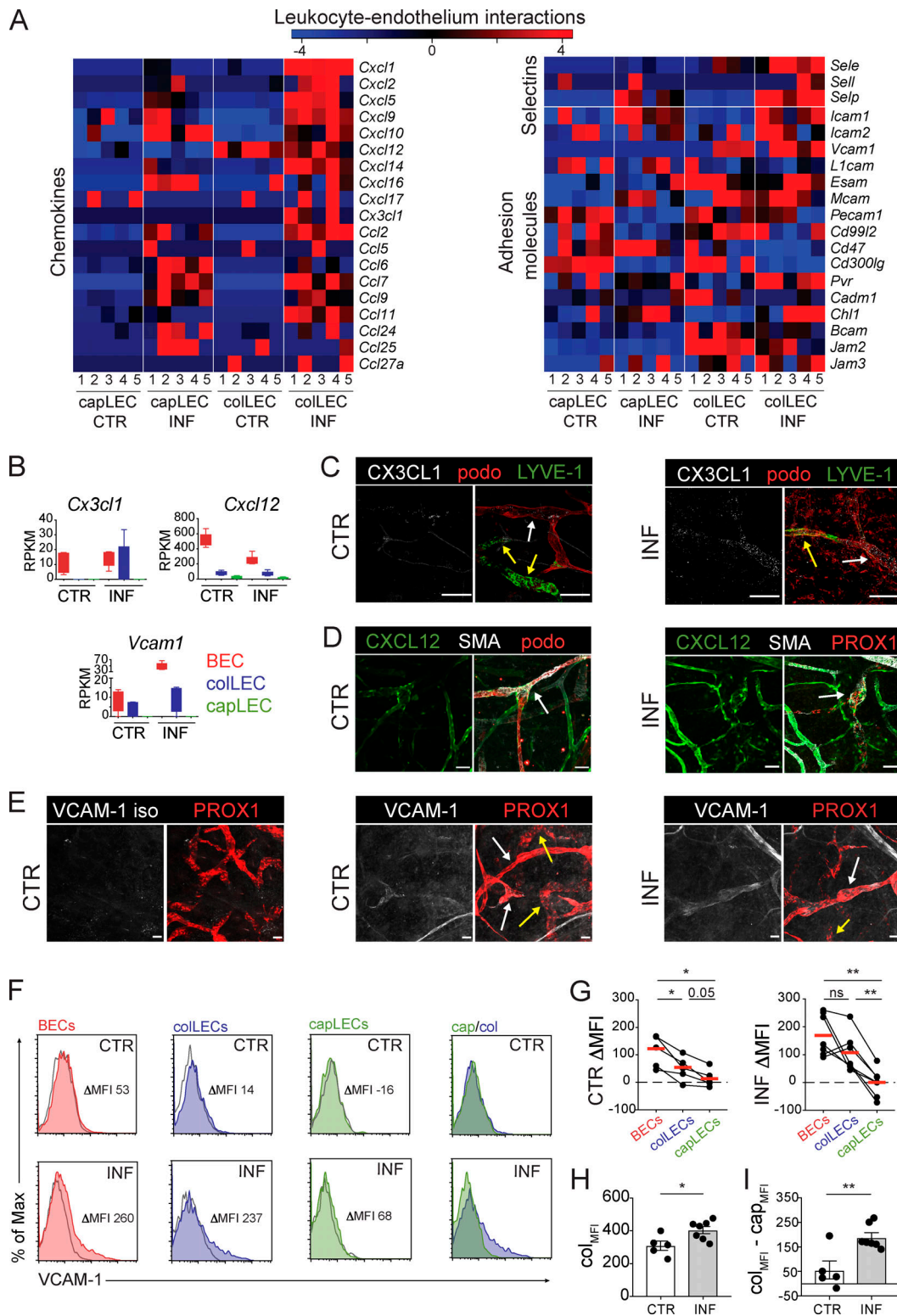


Figure 2. Collector-specific expression of adhesion molecules and chemokines in inflamed lymphatic collectors. (A) Heatmaps of adhesion molecule and chemokine genes involved in leukocyte migration. **(B)** Reads per kilobase per million mapped reads (RPKM) plots of *Cx3cl1*, *Cxcl12*, and *Vcam1* in steady-state (CTR) and INF BECs, colLECs, and capLECs. Box shows median, 25%, and 75% percentile; whiskers show minimum and maximum. Representative whole-mount images showing differential expression of (C) CX3CL1, (D) CXCL12, and (E) VCAM-1 in lymphatic vessels in CTR and INF murine ear skin ($n = 3$ mice per condition). In the case of VCAM-1 (E), the corresponding isotype staining is shown. **(C–E)** White arrows indicate collectors, yellow arrows capillaries. Scale bars, 50 μ m. **(F–I)** Analysis of VCAM-1 expression in single-cell suspensions generated from CTR and INF murine ear skin. **(F)** Representative FACS plots showing VCAM-1 expression in capLECs (CD45⁻CD31⁺podo⁺LYVE-1⁺), colLECs (CD45⁻CD31⁺podo⁺LYVE-1⁺), and BECs (CD45⁻CD31⁺podo⁻LYVE-1⁺) under CTR and INF conditions. Shaded histogram, VCAM-1; empty histogram, isotype control. **(G)** Summary of the delta median fluorescent intensities (Δ MFI): specific-isotype

staining) from all experiments performed under CTR ($n = 5$ mice) or INF ($n = 7$ mice) conditions. Measurements from the same sample are connected by a line. **(H)** Summary of MFIs measured for colLECs in CTR or INF samples. **(I)** Summary of the Δ MFIs measured per experiment between colLECs and capLECs. **(G–I)** Paired one-way ANOVA with Geisser–Greenhouse correction (G) and unpaired Student's t test (H and I); *, $P < 0.05$; **, $P < 0.01$. cap, capillaries; col, collectors; Max, maximum; podo, podoplanin.

(yellow arrows in Fig. 3 I), we also quantified the ratio of DCs attached to the abluminal vessel wall as compared with DCs colocalizing (either inside or outside) with the vessel. This analysis confirmed the accumulation of *Itgbl*^{-/-} DCs around collectors in contrast to capillaries (Fig. 3 K). Taken together, these results functionally confirmed the up-regulation of VCAM-1 in collectors and highlighted the contribution of VCAM-1/integrin β 1 interactions to DC entry into inflamed collectors. In addition to crawl-in studies, we could also confirm the specific contribution of integrin α 4 β 1/VCAM-1 to DC–LEC interactions in vitro adhesion, transmigration, and crawling assays performed with bone marrow-derived DCs and conditionally immortalized LECs (imLECs; Fig. S4).

The BM and ECM surrounding collectors are degraded in inflammation

Our sequencing data had revealed that pathways related to ECM remodeling were enriched in colLECs in inflammation (Fig. 1 I). In line with this observation, we found most matrix metalloproteinases (MMPs) to be strongly up-regulated in inflamed colLECs, while the tissue inhibitors of metalloproteinases (TIMP) 2, 3, and 4 were down-regulated (Fig. 4 A). This suggested that the integrity of the thick and continuous BM surrounding lymphatic collectors might be reduced in inflammation. When quantifying the expression intensities of laminin (Fig. 4 B) and using second harmonic generation (SHG) to detect fibrillar collagen around lymphatic collectors (Fig. 4 C and Videos 5 and 6), we found both to be reduced around inflamed as compared with steady-state collectors. Similarly, laminin and collagen signals around collectors were significantly reduced in ripped ear skin explants after 4 h of culture (Fig. 4, D and E). To address whether ECM remodeling around collectors involved MMPs, we incubated murine ear skin explants in TNF α /IFN γ -containing medium in the presence or absence of the broad spectrum MMP inhibitor prinomastat/AG2240 (PRN), which reportedly is specific for most of the LEC-produced MMPs (i.e., MMP 2, 3, 13, and 14; Fig. 4 A; Butler et al., 2008). Upon PRN treatment, significantly higher SHG signals of fibrillar collagen could be detected around lymphatic collectors (Fig. 4 F), whereas the SHG signal in the interstitial tissue was unaffected (Fig. 4 G).

Blockade of BM/ECM degradation reduces DC entry into collectors

Considering that we found the BM and ECM surrounding collectors to be degraded in inflammation (Fig. 4, B and C) and upon tissue ripping in explants (Fig. 4, D and E), we next asked whether the degradation process might facilitate DC entry into collecting vessels. To address this, we incubated ear skin explants for 4 h in the presence or absence of PRN, to prevent the ripping-induced degradation of laminin and fibrillar collagen, and then performed the crawl-in experiment, by adding DCs for

another 4 h. While PRN treatment did not impact DC entry into capillaries, entry into collectors was significantly reduced (Fig. 4, H and I). Surprisingly, PRN treatment did not reduce the entry of *Itgbl*^{-/-} DCs (Fig. 4, H and J), possibly due to the very low numbers of *Itgbl*^{-/-} DCs identified within lymphatic collectors at this time point, even in absence of PRN treatment (on average, 2.9 *Itgbl*^{-/-} DCs, as compared with 9.7 in the case of WT DCs per image).

Rapid DC migration from inflamed skin to dLNs is integrin dependent

IVM has revealed that DCs and T cells spend hours crawling and patrolling at low speed within lymphatic capillaries before reaching lymphatic collectors, where lymph flow picks up and facilitates their detachment and a greatly accelerated, passive transport to dLNs (Russo et al., 2016; Tal et al., 2011; Teixeira et al., 2017). Our observation of DCs entering into lymphatic collectors in ear skin explants (Figs. 3 and 4 and Videos 2 and 3) and in vivo (Video 4) suggested that degradation of the collector-surrounding ECM and BM and up-regulation of VCAM-1 by colLECs might open up a new, rapid route for DC migration to dLNs in inflammation. By bypassing the slow migration step in capillaries, DCs entering directly into contracting collectors (collector-DCs) would be expected to arrive more rapidly in the dLN as compared with DCs entering through capillaries (capillary-DCs). We therefore next set out to investigate whether interactions between integrin α 4 β 1 on DCs and inflammation-induced VCAM-1 on colLECs might support collector entry and rapid migration to dLNs in vivo.

Previous reports have shown that numbers of adoptively transferred DCs peak in dLN ~2–3 d after transfer (Lappin et al., 1999; Martín-Fontecha et al., 2003). In accordance with our animal protocols for adoptive transfer into inflamed ear skin or footpads, we analyzed DC numbers in the respective draining auricular and popliteal LNs at an early and a later time point after transfer (ear skin: 17 and 40 h; footpad: 14 and 30 h; Fig. 5 A). This analysis confirmed the previously reported migration kinetics by showing that fewer DCs were present in the dLNs at early as compared with late time points after transfer, both under CTR and under INF conditions (Fig. 5, A–C). 5 h after injection, DCs were observed along or within lymphatic capillaries and collectors in proximity to the injection site (Fig. 5 D). We next performed competitive adoptive transfer experiments by injecting 1:1 ratios of fluorescently labeled WT and *Tlnl*^{-/-} DCs into CTR or INF ear skin. When analyzing DCs in the ear-draining auricular LNs at the late time point (i.e., at 40 h after transfer), the ratio of *Tlnl*^{-/-}:WT DCs was significantly reduced under INF as compared with CTR conditions (Fig. 5, E and F), in line with the previously reported integrin dependence of DC migration in inflammation (Johnson et al., 2006; Teixeira et al., 2013) but not in steady-state (Lämmermann et al., 2008). In

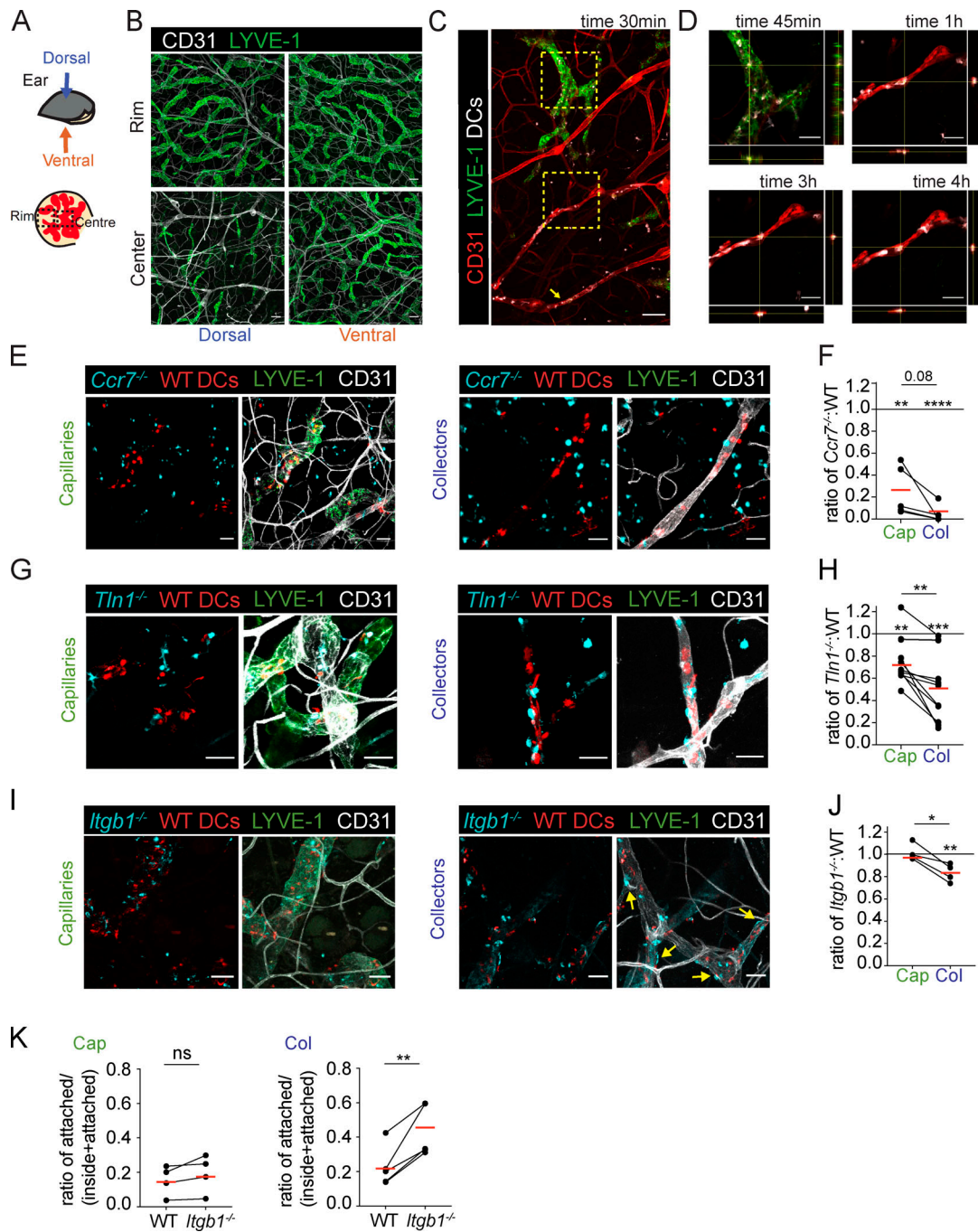


Figure 3. DC entry into lymphatic collectors depends on CCR7, talin1, and integrin $\beta 1$. (A and B) Ears were split along the cartilage and dorsal and ventral whole-mounts stained for CD31 and LYVE-1. (A) Experimental setup. (B) Image of the vascular network at the rim and the center of the dorsal and ventral ear skin. (C and D) Crawl-in experiments: dorsal ear skins were prestained with fluorescent anti-CD31 and anti-LYVE-1 and incubated with LPS-matured DCs and imaged at the indicated time points. Pictures in D were taken in highlighted areas of C. The yellow arrow in C shows where the first sequence of Video 5 was recorded. Representative pictures from five experiments are shown in B–D. (E–K) 1:1 mixtures of fluorescently labeled WT and KO DCs (*Ccr7*^{-/-}, *Tln1*^{-/-}, or *Itgb1*^{-/-}) were incubated on dorsal ears skin explants for 4 h. Explants were stained for CD31 and LYVE-1 before analysis. (E–J) Representative images (E, G, and I) and corresponding quantifications (F, H, and J) of KO:WT DC ratios in capillaries (cap) and collectors (col). (K) Quantification of the ratio of DCs attached to the abluminal side (see yellow arrows in I for *Itgb1*^{-/-} DCs) over total DCs colocalizing (i.e., inside or outside) with the collector. Each dot represents the ratio from one explant (*n* = 4–10 explants per condition). Ratios from the same explant in F, H, J, and K are connected by a line. Statistical significances either compare with the normalized input ratio of 1 or between the groups (connected by lines). (F, H, J, and K) Paired Student’s *t* test. *, *P* < 0.05; **, *P* < 0.01; and ****, *P* < 0.0001.

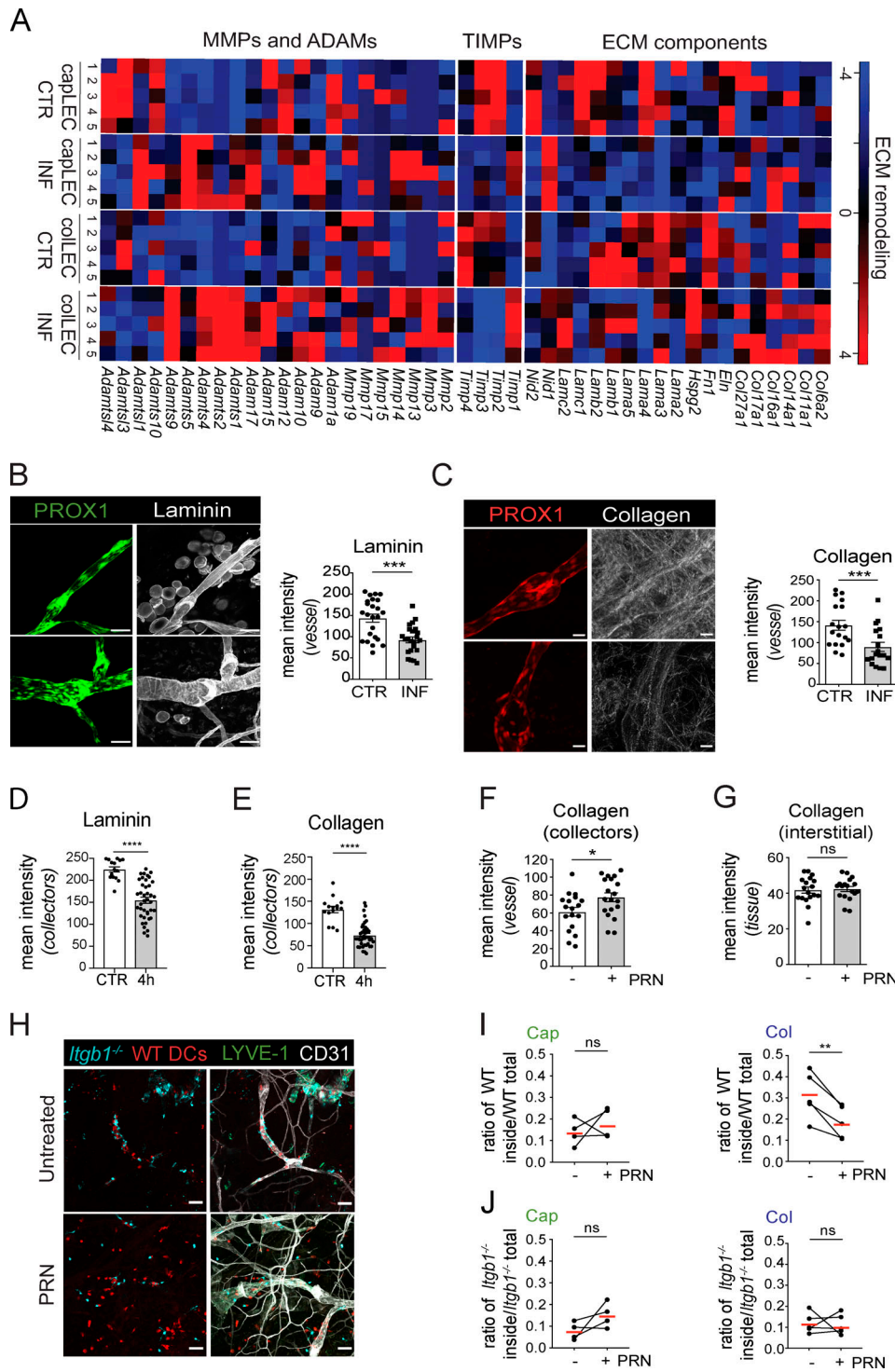


Figure 4. BM degradation and ECM remodeling enhance DC migration. (A) Heatmap of genes involved in BM and ECM remodeling. **(B and C)** Levels of laminin expression and of fibrillar collagen (SHG signal) were analyzed around collectors in CTR and INF ear skin. Representative whole-mount images of PROX1⁺ lymphatic collectors and corresponding quantifications are shown in B for laminin (scale bar, 50 μ m) and C for fibrillar collagen (scale bar, 10 μ m). **(D and E)** Laminin and fibrillar collagen were quantified in ear skin explants at 0 (CTR) and after 4 h of incubation. **(F and G)** Ear skin explants were incubated with TNF α and IFN γ in the presence or absence of PRN. 24 h later, fibrillar collagen levels were quantified (F) around lymphatic collectors and (G) in the tissue. **(B–G)** Pooled data from three whole-mounts per condition in three independent experiments. **(H–J)** Ear skin explants were incubated for 4 h with or without PRN before adding 1:1 mixtures of fluorescent WT and *Itgb1*^{-/-} deficient DCs for 4 h. **(H)** Representative images showing WT and *Itgb1*^{-/-} DCs in capillaries and collectors at the end of the experiment. **(I and J)** Quantification of the impact of PRN treatment on the ratio of DCs inside the vessel, in comparison to all DCs in per image. Results for WT DCs (I) and *Itgb1*^{-/-} DCs (J). Left: Capillaries (cap). Right: Collectors (col). Each dot represents the average from one experiment ($n = 4$ experiments with one or two explants/condition/experiment). Ratios from the same experiment are connected by a line. Scale bars, 50 μ m (B, C, and H). **(B–F)** Unpaired Student's *t* test. **(H and I)** Paired Student's *t* test. *, $P < 0.05$; **, $P < 0.01$; ***, $P < 0.001$; and ****, $P < 0.0001$.

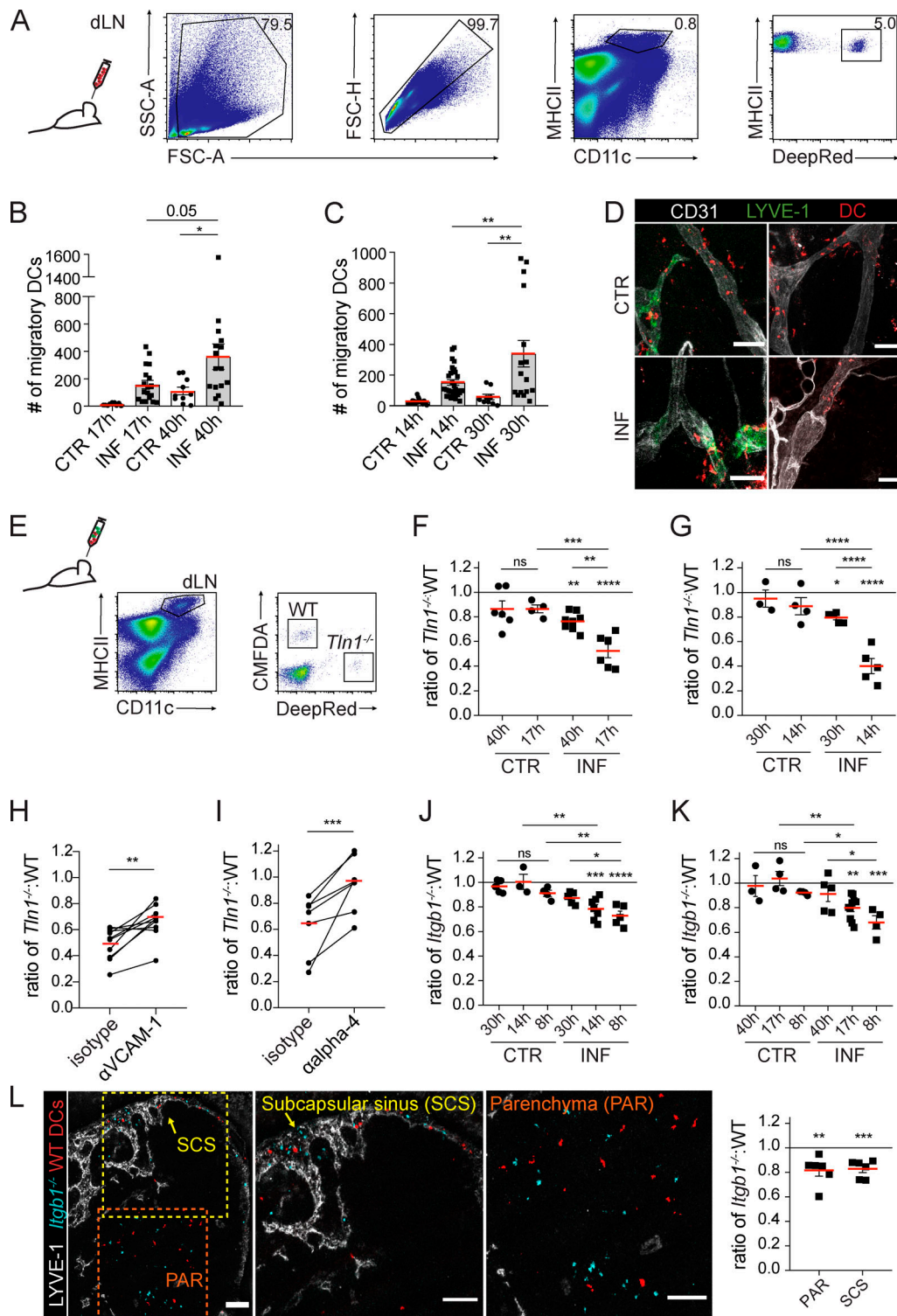


Figure 5. Rapid DC migration from inflamed skin to dLNs is integrin $\beta 1$ dependent. (A–C) Fluorescently labeled WT DCs were injected into INF or CTR mouse ear skin and footpads. DC numbers in dLNs were quantified by FACS at different time points after transfer. (A) Gating scheme. Numbers in graphs show percentage of parent. (B and C) FACS-based quantification of DCs in ear-draining auricular LNs (B) and footpad-draining popliteal LNs (C). Each dot represents the value from one dLN. (D) Representative whole-mounts prepared 5 h after DC injection. Scale bar, 50 μ m. (E–K) 1:1 ratios of differently labeled (F–I) WT and *Tln1*^{-/-} DCs (F–I) or WT and *Itgb1*^{-/-} DCs (J and K) were injected into CTR and INF mouse ear skin or footpads and the DC ratio quantified in the dLNs at different time points after transfer. (E) Representative FACS plots of an ear-draining auricular LN 17 h after DC transfer. (F and G) Analysis of *Tln1*^{-/-}:WT DC ratios in auricular LNs (F) and popliteal LNs (G). (H and I) Impact of anti-VCAM-1 (H) or anti-integrin $\alpha 4$ (I) treatment on the ratio *Tln1*^{-/-}:WT DCs recovered from LNs draining inflamed ears or footpads at 14–17 h after DC transfer. (J and K) Analysis of *Itgb1*^{-/-}:WT DC ratios in footpad-draining popliteal LNs (J) and ear-draining auricular LNs (K). Each dot in F, G, J, and K represents the DC ratio quantified in one dLN of three or four experiments. Each dot in H and I represents the average ratio obtained in 7 or 10 experiments (with 1–3 mice per condition/experiment). Ratios from the same experiment are connected with a line. (L) 1:1

ratios of fluorescent WT and *Itgbl1*^{-/-} DCs were injected into INF mouse footpads and DC ratios quantified in popliteal dLNs 17 h after transfer. Left: Representative picture of a popliteal LN sections at the time of analysis. Middle: Zoom-ins of the subcapsular sinus (SCS) and parenchyma (PAR) areas. All scale bars, 100 μ m. Right: Quantification of the *Itgbl1*^{-/-}:WT DC ratios in the respective area. Each dot represents the ratio in 1 LN (analysis of 5–10 images/LN) of three experiments (two LNs per experiment). Statistical significances either compare with the normalized input ratio of 1 or between the groups. **(B, C, F, G, and H–L)** Unpaired one-way ANOVA followed by Tukey post hoc test (B, C, F, G, J, and K), paired Student's *t* test (H and I), or unpaired Student's *t* test (L). *, *P* < 0.05; **, *P* < 0.01; ***, *P* < 0.001; and ****, *P* < 0.0001. FSC-A, forward scatter area; SSC-A, side scatter area.

comparison to the 40-h time point, DC migration was significantly more talin1 dependent when analyzing dLNs 17 h after transfer, i.e., at the early time point expected to be enriched for the rapidly migrating collector-DCs (Fig. 5 F). A similar time dependence was also observed upon DC transfer into inflamed footpads (Fig. 5 G). When adoptively transferring 1:1 ratios of *Tln1*^{-/-}:WT DCs into inflamed skin in the presence of either VCAM-1- or integrin α 4- blocking antibodies, the ratio of *Tln1*^{-/-}:WT DCs in dLNs was significantly increased, providing an additional confirmation of the involvement of VCAM-1/integrin α 4 β 1 interactions in this process (Fig. 5, H and I).

Rapid DC migration from inflamed skin to dLNs is integrin β 1 dependent

To specifically address the integrin β 1 dependence of DC migration in inflammation, we adoptively transferred 1:1 ratios of fluorescently labeled WT and *Itgbl1*^{-/-} DCs into footpads (Fig. 5 J). Analysis of the DC ratio in popliteal LNs at early (i.e., 8 and 14 h) and late time points (i.e., 30 h) after transfer indicated no contribution of integrin β 1 to DC migration under steady-state conditions (Fig. 5 J). Conversely, upon transfer of DCs into inflamed footpads, the ratio of *Itgbl1*^{-/-}:WT DCs in popliteal LNs was significantly reduced at the early time points analyzed, i.e., 8 or 14 h after transfer (Fig. 5 J). A similar time dependence for β 1 integrin requirement in inflammation-induced DC migration was observed upon transfer into the inflamed ear skin and analysis of the ear-draining auricular LN (Fig. 5 K). When analyzing the localization of adoptively transferred DCs in LNs draining INF skin by confocal microscopy, a reduction in the ratio of *Itgbl1*^{-/-}:WT DCs was found both in the subcapsular sinus as well as in the LN parenchyma (Fig. 5 L). This demonstrated that the inflammation-induced impairment of *Itgbl1*^{-/-} DCs in rapidly migrating to dLNs detected by FACS (Fig. 5, J and K) was not due to a potential defect in crossing the subcapsular sinus floor, but originated from impaired entry into afferent lymphatics.

Loss of VCAM-1 in lymphatic collectors reduces rapid DC migration

To address whether collector entry and rapid migration of endogenous DCs also depend on integrin α 4 β 1/VCAM-1, we generated *Prox1-Cre^{ERT2} Vcam1^{fl/fl}* mice, i.e., conditional knockouts, in which VCAM-1 deletion is specifically induced in LECs upon treatment with tamoxifen (Fig. S5, A–C). To induce inflammation in this mouse model, the phorbol ester 12-O-tetradecanoylphorbol-13-acetate (TPA) was topically applied to the ear skin of tamoxifen-treated Cre⁺ (*Prox1-Cre^{ERT2} Vcam1^{fl/fl}*) and Cre⁻ control mice (WT or *Vcam1^{fl/fl}*). Whereas in Cre⁻ control mice, TPA treatment induced VCAM-1 expression in BECs and colLECs,

VCAM-1 was up-regulated in BECs but not in colLECs of Cre⁺ mice (Fig. S5, D–F). To assess migration of endogenous DCs in this model, we again induced inflammation by topical application of TPA (Fig. 6 A). 24 h later, the ear skin was painted with the contact sensitizer FITC. When analyzing the ear-draining auricular LNs 18 h after FITC painting, the number and percentage of FITC⁺ migratory DCs (MHCII⁺ CD11c⁺) were significantly reduced in Cre⁺ as compared with Cre⁻ mice, demonstrating that loss of VCAM-1 in collectors resulted in a defect in rapid DC migration, which likely involved entry via collectors (Fig. 6, B–D). Conversely, no difference in the numbers of FITC⁻ migratory DCs was observed, indicating no general defect in the migration of DCs that had exited the skin before FITC application and consequently were expected to contain a higher fraction of slowly migrating capillary-DCs (Fig. 6, B, E, and F). Last but not least, to investigate whether, in absence of LEC-expressed VCAM-1, inflammation-induced DC entry into collectors was compromised, we performed crawl-in experiments with WT DCs in ear skin explants of Cre⁺ or Cre⁻ mice. When analyzing confocal images, the ratio of DCs within capillaries compared with all DCs in the selected image was similar in Cre⁺ and Cre⁻ mice, indicating no entry defect. By contrast, this ratio was significantly reduced in collectors (Fig. 6, G and H). Similarly, DCs were found to accumulate outside of collectors but not outside of capillaries in Cre⁺ mice, confirming a collector entry defect in absence of VCAM-1 expression (Fig. 6, G and I). Overall, these results identify lymphatic collectors as a new site supporting rapid, integrin α 4 β 1/VCAM-1-mediated DC migration in inflammation.

Discussion

In this study, we have identified lymphatic collectors as an inflammation-induced entry site for DCs migrating to dLNs. Our findings on one hand challenge the current paradigm of lymphatic trafficking, which thus far has assumed that entry occurs exclusively at the level of lymphatic capillaries. On the other hand, by revealing the connection between capillary- versus collector-entry and the overall speed of DC migration, our results contribute to a better understanding of the kinetics of DC migration to dLNs.

Based on the anatomy of lymphatic capillaries, i.e., their discontinuous BM and the characteristic open flaps between neighboring LECs (Baluk et al., 2007), as well as on experimental findings from crawl-in studies in explants (Pflücke and Sixt, 2009) and IVM (Nitschké et al., 2012; Tal et al., 2011), capillaries have been considered the exclusive entry site into afferent lymphatics. Considering that lymphatic collectors are surrounded by LMCs, a thick BM, and feature tight junctions

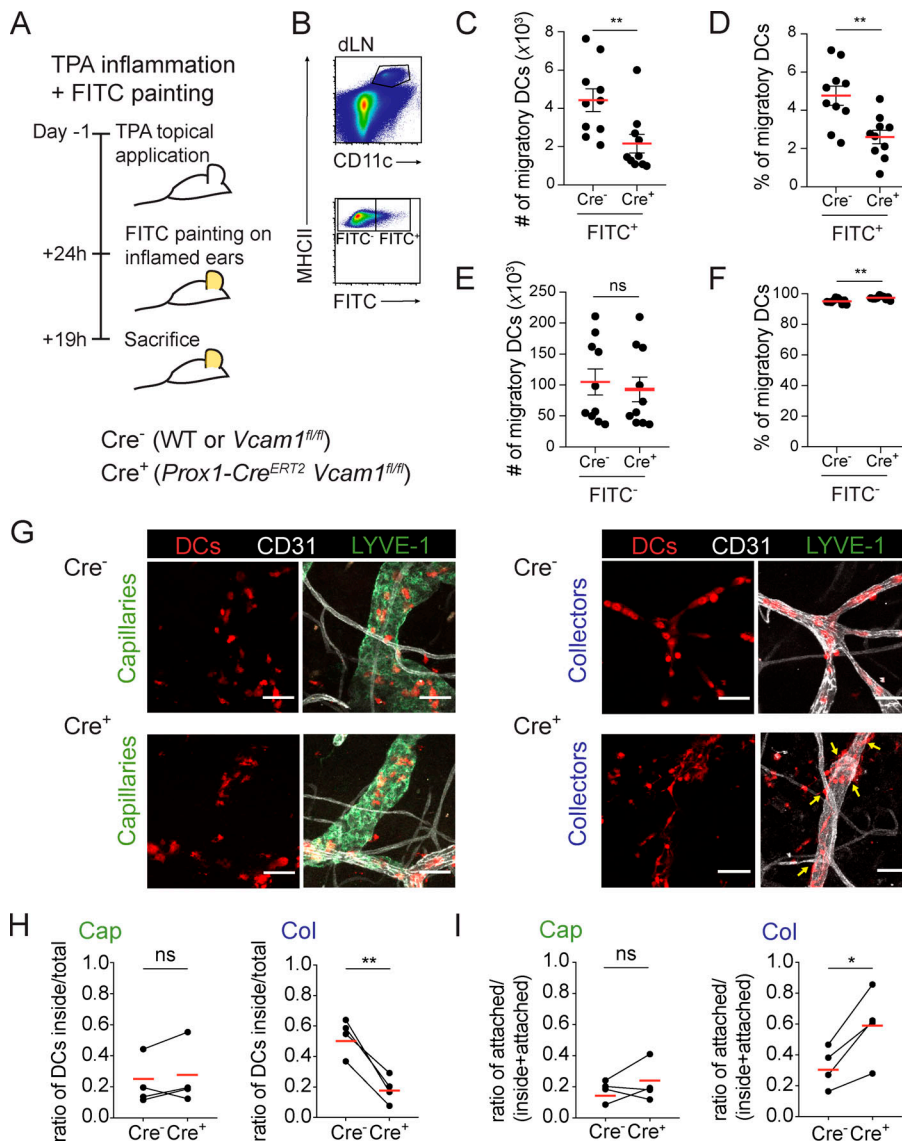


Figure 6. Loss of VCAM-1 in lymphatic collectors reduces rapid DC migration. (A–F) A FITC painting experiment was performed in the TPA-inflamed ears of tamoxifen-treated Cre⁺ (*Prox1-Cre^{ERT2} Vcam1^{fl/fl}*) and Cre⁻ (WT or *Vcam1^{fl/fl}*) mice. **(A)** Schematic depiction of the experiment. **(B)** FACS gating scheme on auricular LNs. **(C–F)** Analysis of absolute numbers (C and E) and percentages (D and F) of FITC⁺ (C and D) and FITC⁻ (E and F) migratory (CD11c⁺ MHCII⁺) DCs. Pooled data from two similar experiments are shown (*n* = 10 mice per group). Each dot represents a value from one mouse. **(G–I)** Crawl-in experiments were performed with WT DCs in ear skin explants of Cre⁺ and Cre⁻ mice. **(G)** Representative images of DCs in and around capillaries and collectors. Scale bars, 50 μm. Yellow arrows show DCs that did not enter but remained attached to the abluminal side of the collector. **(H)** Quantification of the ratio of DCs inside the vessel, in comparison of all DCs counted per image. Left: Capillaries (cap). Right: Collectors (col). **(I)** Quantification showing the ratio of DCs attached to the abluminal side over all DCs colocalizing (i.e., inside or outside) with the vessel. Average ratios of all the images analyzed in the same experiment (*n* = 4 experiments; two or three explants/condition/experiment) are connected by a line. **(C–F)** Unpaired Student's *t* test. **(H and I)** paired Student's *t* test. *, *P* < 0.05; and **, *P* < 0.01.

between neighboring COLLECs, it might seem less intuitive that cell entry would also occur at this site. However, it is well known that leukocytes continuously extravasate from blood vessels, a process that requires transmigration through tight endothelial junctions and passage through a thick BM and a vessel-surrounding pericyte layer (Nourshargh et al., 2010). Thus, in spite of greater ease of entering into capillaries, entry into collectors should not present an unsurmountable obstacle to leukocytes. A likely reason why collector entry was not observed in the initial report of DC entry into capillaries in explants (Pflücke and Sixt, 2009) could be that those studies were performed in the ventral ear halves, which, in contrast to the dorsal halves used in our explant studies, contain mostly capillaries and almost no collectors (Fig. 3 B).

Our crawl-in and time-lapse imaging experiments in explants revealed that entry into collectors required more time compared with entry into capillaries, likely because of the thicker BM and tight cell junctions in collectors. In support of the barrier function that the collector-surrounding ECM and BM pose to leukocytes, we found that DC entry into lymphatic

collectors in explants was significantly reduced in the presence of the broad MMP inhibitor PRN. While the passage of epidermal DCs through the thick subepithelial BM was shown to depend on MMP-mediated proteolysis (Ratzinger et al., 2002), pore generation in the much thinner capillary-surrounding BM and DC entry into lymphatic capillaries was not affected by MMP blockade (Pflücke and Sixt, 2009). However, the fact that collectors are embedded in a much thicker BM and fibrillar collagen layer than capillaries might explain why we found fewer DCs inside collectors in crawl-in experiments upon MMP inhibition. In spite of the fact that transmigration into explant collectors took longer than into capillaries, our *in vivo* migration studies indicated that collector entry nevertheless shortens the overall time DCs require to migrate from a peripheral tissue to a dLN. Our explanation for this is that DCs entering directly into collectors manage to avoid the long time otherwise spent in capillaries, where their speed of active migration would be several log units lower than the speed of passive transport in contracting dermal collectors (Russo et al., 2016; Teixeira et al., 2017). Future studies will need to address whether collector

entry and rapid migration are mechanisms used by all DCs or only by specific DC subsets, for instance, dependent on their localization in the tissue and chemotactic requirements (Clausen and Stoitzner, 2015).

Even though CCL21 was produced less by cOLECs than by capLECs (Fig. S3, A and B; Reynolds et al., 2021; Russo et al., 2016), DC entry into collectors in explants was highly CCR7 dependent. Interestingly, we observed that two other chemokines with reported roles in DC migration were preferentially up-regulated in inflamed cOLECs and/or expressed in cOLEC-surrounding LMCs, namely CX3CL1 (Johnson and Jackson, 2013) and CXCL12 (Kabashima et al., 2007), respectively. It is likely that these chemokines act in concert with CCL21 in recruiting DCs toward and into lymphatic collectors under inflammatory conditions. In agreement with the collector-entry kinetics that we observed for *Itgbl^{-/-}* DCs, the impact of blocking CXCL12 or CX3CL1 signaling in DCs reportedly was more pronounced at early as compared with late time points (Johnson and Jackson, 2013; Kabashima et al., 2007). This further suggests that CXCL12 and CX3CL1, in analogy to VCAM-1, contribute to collector entry of DCs. At present, we do not know what the potential functional relevance of collector entry might be. It is perceivable that a more rapid arrival and induction of adaptive immunity in dLNs could be advantageous in the context of infections with rapidly proliferating and spreading pathogens. On the other hand, increasing evidence suggests that LECs exert immune-modulatory functions (Garnier et al., 2019) and express molecules that may dampen DC maturation (Christiansen et al., 2016; Podgrabinska et al., 2009). Entry into collectors might therefore allow avoiding the long time spent in direct contact with LECs in the capillary compartment and impact the DC's immunostimulatory phenotype. In any case, the fact that the migration defect observed upon loss of VCAM-1 or of ITGB1 followed a clear time dependence indicates that this route of migration is only used by a fraction of DCs. At later time points of analysis, this defect is overridden by the bulk of DCs, which most likely entered via lymphatic capillaries. Future studies will therefore need to address both the relative contribution and functional relevance of collector entry.

Preferential up-regulation of VCAM-1 in collectors was not only observed by immunofluorescence and FACS, but also indirectly demonstrated by our crawl-in experiments in ear skin explant, where integrin β 1-deficient DCs were compromised in their entry into collectors but not into capillaries. Interestingly, besides DCs, the lymphatic migration of activated CD4⁺ T cells (Teijeira et al., 2017) and of regulatory T cells (Brinkman et al., 2016) in inflammation was also shown to depend on VCAM-1. This suggests that rapid migration to dLNs by entry into collectors is a mechanism used by various types of migrating leukocytes. The fact that we also detected α SMA-covered lymphatic vessels in the lower dermis of human skin, as previously reported (Wang et al., 2014), could suggest that DC entry into collectors and its resulting impact on DC migration kinetics is also relevant in humans. At the same time, it is worth mentioning that a vast plasticity and heterogeneity exists in the lymphatic vasculature of different organs, and the separation into capillaries and collectors does not apply to all vascular beds

(Petrova and Koh, 2018). It will therefore need to be investigated whether collector entry as a route for rapid migration, which we so far identified in footpad and ear skin, also occurs in other tissues.

Materials and methods

Data availability

The RNA sequencing data generated during this study are available at ArrayExpress under accession no. E-MTAB-9175.

Mice

WT C57BL/6 mice were purchased from Janvier. *Prox1-eGFP* (Choi et al., 2011), *CXCL12-GFP* (Ara et al., 2003), and *Ccr7^{-/-}* (Förster et al., 1999) mice were bred in our facility. *Prox1-mOrange2 CD11c-eYFP* were generated by crossing *Prox1-mOrange2* (Hägerling et al., 2011) with *CD11c-eYFP* (Lindquist et al., 2004). *Prox1-Cre^{ERT2} Vcam1^{fl/fl}* mice were generated by crossing *Vcam1^{fl/fl}* mice (Koni et al., 2001) with *Prox1-Cre^{ERT2}* mice (Bazigou et al., 2009). To induce VCAM-1 deficiency, 6–8-wk-old *Cre⁺ (Prox1-Cre^{ERT2} Vcam1^{fl/fl})* or *Cre⁻* control mice (WT or *Vcam1^{fl/fl}*) were injected i.p. on five consecutive days with tamoxifen (Sigma-Aldrich; 1 mg/20 g, dissolved in sunflower seed oil). With the exception of *CXCL12-GFP* mice (OHB), all animals were housed and experiments were performed under specific pathogen-free conditions. All experiments were approved by the Cantonal Veterinary Office Zurich under Project Licenses ZH268/14, ZH237/2016, and ZH239/19.

For the generation of *Tln1^{-/-}* bone marrow-derived DCs, *Mxl1-Cre^{+/+} Tln1^{fl/fl}* mice or controls were injected i.p. with 250 μ g Poly (I)-Poly (C) (GE Healthcare), and bone marrow was harvested 12–14 d later (Kühn et al., 1995; Petrich et al., 2007). For the generation of *Itgbl^{-/-}* bone marrow-derived DCs, bone marrow was harvested from *Vav1-iCre^{+/+} Itgbl^{fl/fl}* or control mice (de Boer et al., 2003; Potocnik et al., 2000). *Cre⁻* littermates were used as controls and are referred to as WT. Experiments for the induction of *Tln1^{-/-}* were approved by the District Government of Bavaria (ROB-55.2-2532.Vet_02-15-96).

Induction of a CHS response in the ear skin or footpad

This experiment was described by Vigl et al. (2011). Briefly, 7–8-wk-old C57BL/6 females were sensitized by topical application of 2% oxazolone (Sigma-Aldrich) on shaved abdomen and paws; 5 d later, 1% oxazolone was applied on ears or footpads, and 24 h later, animals were sacrificed, and dLNs or skin tissue were harvested.

FACS sorting and RNA extraction

INF and uninflamed ears from individual animals were cut into small pieces and enzymatically digested in a 4-ml mixture of 10 mg/ml collagenase IV (Thermo Fisher Scientific), 5 mg/ml dispase II (Sigma-Aldrich), 0.1 mg/ml DNase I (Roche), and 1 mM CaCl₂ (Sigma-Aldrich) in PBS (Thermo Fisher Scientific) at 37°C for 15 min in rotation. Suspensions were passaged through a 40- μ m cell strainer (BD Biosciences), and resulting single-cell suspensions were stained at 4°C with APC/Cy7 anti-mouse CD45 (BioLegend), PE anti-mouse CD31 (BioLegend), APC anti-mouse

Podoplanin (BioLegend), AF488 anti-mouse LYVE-1 (eBioscience), and 7-AAD (BioLegend). After excluding doublets and dead cells, the different EC populations (~30,000 BECs, ~5,000 colLECs, and ~2,500 capLECs per mouse/condition) were isolated on a FACS Aria Cell Sorter (70- μ m nozzle) using BD FACSDiva software (both BD Biosciences) and sorted into PicoPure RNA extraction buffer (Thermo Fisher Scientific). RNA was isolated and genomic DNA was eliminated using the PicoPure RNA isolation kit (Thermo Fisher Scientific). RNA quality and concentration were analyzed with a Bioanalyzer (Agilent Technologies), and samples of the same animal with RNA integrity number >7 and minimum concentration of 200 ng/ml were further processed for RNA sequencing.

RNA sequencing and data normalization

cDNA libraries were generated using Ovation Single Cell RNA-Seq System (NuGen), and the quality and concentration of resulting libraries were assessed with a bioanalyzer. RNA sequencing and differential expression analysis were performed by Functional Genomics Center Zurich. BECs, colLECs, and capLECs generated libraries from the same mouse ($n = 5$ INF mice, and $n = 5$ CTR mice) were sequenced using an Illumina HiSeq System. Sequencing depth was at least 10 million read counts per sample, and differential gene expression analysis was done using DESeq2 (defined threshold as \log_2 fold change >0.5; P value <0.01). Principal component analysis was performed using “DESeq2,” visualized with “ggplot2” in R v3.6.1. The two principal components explaining most of the variation in our data were plotted against another, allowing us to cluster our samples in distinct groups. Gene expression heatmaps were generated using the “ezRun” and “heatmaply” packages (Galili et al., 2018) in R. Euler diagrams were generated with the R “eulerr” package. Pathway analysis was performed using the MetaCore Process Network (Clarivate Analysis) with a cutoff of fold change >1.5 and P value <0.05.

CCL21 and talin1 gene expression

For CCL21 experiments, CTR and INF ears from two mice per condition were pooled, enzymatically digested, and FACS-sorted as described above. Extracted and purified RNA (PicoPure RNA isolation kit; Thermo Fisher Scientific) was converted and amplified into cDNA using the Ovation Pico WTA System V2 (NuGen). For talin1 experiments, RNA from LPS mature DCs previously isolated from the bone marrow of *Mxl-Cre^{+/-} Tln1^{fl/fl}* mice was extracted and converted into cDNA. Quantitative PCR analyses of *Ccl21* (*Ccl21* Mm0364971_m1; *ACTB*, both Thermo Fisher Scientific) and *Tln1* (*Tln1* forward: 5'-GGCCCTCCCAAC GACTTT-3', reverse: 5'-AGCCTCTAGCCAGATGCCTTT-3'; *Rpl0* forward: 5'-AGATTCGGGATATGCTGTTGG-3', reverse: 5'-TCG GGTCTAGACCAGTGTTTC-3') gene expression were performed on a Fast Real-time PCR system (Thermo Fisher Scientific).

Whole-mount immunofluorescence and analysis

Mouse ears were harvested, split, and fixed for 2 h in 4% paraformaldehyde (PFA) at room temperature (RT). Subsequently, whole-mounts were incubated overnight with the following primary antibodies: rat anti-mouse CD31 (BD Bioscience), rabbit

anti-mouse LYVE-1 (AngioBio), anti- α SMA coupled to Cy3 (Sigma-Aldrich), anti- α SMA eFluor660 (eBioscience), goat anti-human PROX1 (R&D Systems), hamster anti-mouse Podoplanin (clone 8.1.1; Developmental Studies Hybridoma Bank, University of Iowa), rabbit anti-mouse laminin (Sigma-Aldrich), goat anti-mouse VCAM-1 (R&D Systems), rabbit anti-mouse CX3CL1 (Thermo Fisher Scientific), rat anti-mouse VE-cadherin (R&D Systems), and goat anti-mouse CCL21 (R&D Systems). The next day, whole-mounts were incubated for 2 h with Alexa Fluor 488-, 594-, or 647-conjugated secondary antibodies (Invitrogen) and mounted in Mowiol (Sigma-Aldrich). Whole-mount Z-stacks were acquired either on a Leica TCS SP8 (Leica Microsystems) or on a Zeiss 880 confocal microscope (Carl Zeiss AG). Fibrillar collagen signal was detected by SHG on the MP Leica TCS SP8. Images were acquired using the Leica Application Suite LASX software (version 3.5.5.19976; Leica Microsystems) or the ZEN software (version 2.3; Carl Zeiss AG), respectively. Image analysis and quantification were performed with ImageJ (National Institutes of Health). For image-based quantifications, 10–20 pictures for whole-mount were taken. Regions of interest in each projected Z-stack were selected based on PROX1, CD31, and LYVE-1 stainings and applied in our channel of interest to obtain mean intensity values. Areas containing blood vessels or other positive structures besides lymphatics were excluded. To assess laminin and SHG in explants, freshly harvested dorsal halves were cultured in leukocyte medium for 4 h or 24 h in the presence of 10 ng/ml TNF α (R&D Systems) and IFN γ (Peprotech), and treated with 10 μ M PRN (Sigma-Aldrich) or vehicle (water). Ear whole-mounts were prepared subsequently, and SHG and laminin were analyzed as described above.

For extracellular CCL21 stainings, ear halves were blocked for 2 h in 0.1% BSA/PBS and stained with primary antibodies in 0.1% BSA/PBS at 4°C (CD31, CCL21, and LYVE-1, as described above) overnight. Secondary antibody staining in PBS, mounting, and imaging were performed as described above.

Immunofluorescence staining on human skin tissue

O.C.T.-embedded human healthy skin samples were snap-frozen in liquid nitrogen, and 8- μ m cryostat sections were prepared. After fixation with 4% PFA for 10 min at RT, sections were blocked with PBS containing 5% donkey serum, 0.1% Triton X-100, and 1% BSA for 1 h at RT, followed by incubation with mouse anti-human podoplanin (Agilent; clone D2-40) and polyclonal rabbit anti-human LYVE-1 (Reliatech) antibodies overnight at 4°C. After abundant washes with PBS, sections were incubated with donkey anti-mouse Alexa Fluor 647 and donkey anti-rabbit Alexa Fluor 488 secondary antibodies (Thermo Fisher Scientific) together with Hoechst 33342 (Thermo Fisher Scientific) for 30 min at RT. After abundant washes with PBS, sections were incubated with anti-human α SMA-Cy3 antibody (Sigma-Aldrich) for 2 h at RT. Sections were washed with PBS and mounted with Mowiol mounting medium (Sigma-Aldrich). Images were acquired using a panoramic 250 Flash III digital Slide Scanner (3D Histech). Human studies were approved by the local ethics committee (Kantonale Ethikkommission Zürich,

approval 2017-00687), and informed consent was obtained from participants.

FACS analysis on ear and footpad skin and explants

Cell suspensions were prepared as described (Vigl et al., 2011). Briefly, ear or footpad skin was cut into small pieces and digested with 4 mg/ml collagenase IV (40 min, 37°C; Invitrogen), followed by passage through a 40- μ m cell strainer (BD Biosciences).

In the case of VCAM-1 staining, Fc receptors were blocked by incubating dermal cell suspensions for 10 min at 4°C with rat anti-mouse CD16/32 (10 μ g/ml; BioLegend). Next, the following antibodies were for 30 min at 4°C: APC/Cy7 rat anti-mouse CD45 (BioLegend), BV421 rat anti-mouse CD31 (BioLegend), APC Syrian hamster anti-mouse Podoplanin (BioLegend), Alexa Fluor 488 rat anti-mouse LYVE-1 (eBioscience), Zombie Aqua (dilution as recommended by manufacturer, BioLegend), and Alexa Fluor 647 rat anti-mouse VCAM-1 (BioLegend) or Alexa Fluor 647 isotype antibody rat IgG2a (BioLegend). All antibodies were added at a final concentration of 2.5 μ g/ml in FACS buffer (PBS containing 2% FCS [Thermo Fisher Scientific] and 2 mM EDTA [Sigma-Aldrich]). After incubation, cells were washed twice with PBS, followed by FACS acquisition on a CytoFlex S using CytExpert software (both Beckman Coulter) and analyzed using FlowJo software 10.4.1 (Tree Star).

For the expression analysis of other endothelial proteins, the following panel was used: APC/Cy7 rat anti-mouse CD45 (BioLegend), BV421 rat anti-mouse CD31 (BioLegend), APC or PE Syrian hamster anti-mouse Podoplanin (BioLegend), Alexa Fluor 488 rat anti-mouse LYVE-1 (eBioscience), and Zombie Aqua (BioLegend). Targets were detected with the following antibodies: APC rat anti-mouse endothelial cell adhesion molecule, APC Armenian hamster anti-mouse ITGB3, Alexa Fluor 647 rat anti-mouse MRC1, and PE rat anti-mouse ICAM-1 (all from BioLegend).

Bone marrow–derived DCs

DCs were generated from bone marrow extracted from tibia and femurs of mice as described by Lutz et al. (1999). Briefly, red blood cells were lysed with ACK buffer (4.01 g NH₄Ac, 0.5 g KHCO₃, and 0.01 g EDTA in 500 ml H₂O, all from Sigma-Aldrich). 5 × 10⁶ cells were plated into bacterial dishes (Greiner Bio-One) in 10 ml of DC medium (leukocyte medium + GM-CSF) containing RPMI 1640 (Sigma-Aldrich), 10% FCS, 15 mM Hepes, 1 mM sodium pyruvate, penicillin (100 U/ml), streptomycin (100 μ g/ml), L-glutamin (2 mM; all from Thermo Fisher Scientific), 50 μ M β -mercaptoethanol (Sigma-Aldrich), and 80 ng/ml GM-CSF (derived from the supernatant of hypoxanthine-aminopterin-thymidine-sensitive Ag8653 myeloma cells [X63 Ag8.653] transfected with murine GM-CSF cDNA3; Zal et al., 1994). On day 9, the floating cell fraction was harvested and reseeded into tissue-culture–treated dishes (TPP) in DC medium containing 0.1 μ g/ml LPS (Enzo Life Sciences). Floating DCs were harvested 24 h later, and DC purity, maturation status, and integrin expression were analyzed by FACS using PE/Cy7 Armenian hamster anti-mouse CD11c, BV421 rat anti-mouse MHC-II, APC rat anti-mouse CD86, FITC Armenian hamster anti-mouse CD80, AF647 rat anti-mouse CD11a, FITC Armenian hamster anti-mouse CD29, AF647 rat anti-mouse CD49d, FITC rat anti-mouse CD18, and corresponding isotype controls (all from BioLegend).

Crawl-in experiments

LPS-matured BM-DCs from WT, *Ccr7*^{-/-}, *Mxl-Cre*^{+/-} *Thn1*^{fl/fl}, and *Vav-iCre*^{+/-} *Itgbi*^{fl/fl} mice were generated as described above. 40,000 cells labeled with 5-chloromethylfluorescein diacetate (CMFDA) or DeepRed (DR; Thermo Fisher Scientific; ratio 1:1) in 40 μ l leukocyte medium were added into the dermis of ear explants and incubated at 37°C, 5% CO₂, for 15–60 min. After removing nonadherent cells, explants were further incubated 3 h in the presence of leukocyte medium. In some cases, explants were treated 4 h with 10 μ M PRN (Sigma-Aldrich) or vehicle (water) prior the addition of DCs. Crawl-in experiments in *Cre*⁺ (*Prox1-Cre*^{ERT2} *Vcam1*^{fl/fl}) or *Cre*⁻ control mice (WT or *Vcam1*^{fl/fl}) ears were performed with 80,000 WT DC cells labeled with CMFDA or DR following the protocol described above. Ear whole-mounts were prepared by fixing explants with 2% PFA for 30 min at RT, staining with PE rat anti-CD31 and biotin-streptavidin PerCP/Cy5.5 rat anti-LYVE-1 for 30 min at RT, and mounting in Mowiol (Calbiochem). Cells inside lymphatic collectors and lymphatic capillaries were counted in ImageJ using the orthogonal view from 15–20 pictures per whole-mount taken with the microscopes aforementioned.

Time-lapse imaging

IVM was performed on the dorsal side of INF ears of anesthetized mice using a Leica SP8 MP microscope with an inverted 25× 0.95 NA objective, as described previously (Hunter et al., 2019; Teixeira et al., 2017). Ex vivo imaging in the dorsal side of ear skin explants was performed on an Olympus upright confocal microscope at 37°C, 5% CO₂, and acquired using Olympus FV31S-SW (version 2.3.1.163; Olympus Corporation) or on a Zeiss 780 confocal microscope (Carl Zeiss AG) with an inverted 10× or 20× objective using the ZEN software (version 2.3; Carl Zeiss AG). In these experiments, ear explants from *Prox1-mOrange2* were stained with eFluor660 or Alexa 488 rat anti-mouse LYVE-1 (eBiosciences). WT mice were additionally stained with PE rat anti-mouse CD31 in leukocyte medium for 30 min at 37°C, 5% CO₂, before adding CMFDA- or DR-labeled DCs.

Culture of imLECs

Conditionally imLECs expressing a heat-labile version of the large T antigen (Vigl et al., 2011) were cultured at 33°C on collagen (Advanced Biomatrix) and fibronectin (Nutacon)–coated dishes (10 μ g/ml each) in media containing 40% DMEM (low glucose), 40% F12-Ham, 20% FBS (all from Gibco), 56 μ g/ml heparin (Sigma-Aldrich), 10 μ g/ml endothelial cell growth supplement (Sigma-Aldrich), antibiotic antimycotic solution (1×; Fluka), and L-glutamine (2 nM; Fluka). Additionally, murine IFN γ (1 U/ml; Peprotech) was added to induce large T-antigen expression (Vigl et al., 2011).

For experimental assays, imLECs were seeded onto the specific chamber/plate on collagen and fibronectin coating at 37°C without IFN γ . After 24 h, media were exchanged for 2% FBS starvation media, and cells were cultured for 6–8 h, after which TNF α and IFN γ (both 10 ng/ml) were added, and cells were cultured for an additional 16–18 h before experiments. For ICAM-1 and VCAM-1 expression, FITC rat anti-mouse ICAM-1 and AF647 rat anti-mouse VCAM-1 and corresponding antibody

isotypes were used (all from BioLegend). All blocking experiments in vitro with DCs were performed using anti-ICAM-1 (10 $\mu\text{g/ml}$; YN1/1.7.4; Biolegend), anti-VCAM-1 (25 $\mu\text{g/ml}$; 6C7.1), or anti-integrin $\alpha 4$ (10 $\mu\text{g/ml}$; PS/2) blocking antibodies or corresponding isotype controls rat IgG2b (Biolegend), rat IgG1 (BioXCell), and rat IgG2b (BioXCell), respectively.

In vitro cell crawling experiments

imLECs were seeded into coated channeled chamber slides (μ -Slide VI^{0.4}; IBIDI). On the day of the assay, monolayers were preblocked with blocking antibodies for 30 min followed by the addition of 30,000 DCs, with or without blocking antibody. After 20 min, chambers were rinsed twice with media to remove nonadherent DCs. After a further 10 min equilibration at 37°C, time-lapse imaging was performed on a fluorescent microscope (Nikon Eclipse Ti-E) equipped with a Hamamatsu ORCA-Flash4.0 charge-coupled device camera (Hamamatsu) and a 20 \times objective (0.75 NA; Nikon). Phase contrast and FITC and APC fluorescence images were captured every 30 s for 30 min. Videos were analyzed using IMARIS software.

In vitro transmigration assay

imLECs were seeded onto the upper side of coated Transwell membrane inserts with 5- μm pore size (Corning Life Sciences) and grown to confluence. On the day of the assay, CCL21 (100 ng/ml; Peprotech) was added in the bottom well of the Transwell. imLEC monolayers were preblocked or not with blocking antibodies for 1 h followed by the addition of 50,000 labeled WT DCs or 1:1 ratios of differently labeled *Tln1*^{-/-}:WT or *Itgbl*^{-/-}:WT, with or without blocking antibody, in the upper well of the Transwell insert. After 4 h, the medium in the bottom well was collected and the number of DCs quantified by flow cytometry on a CytoFlex S (Beckman Coulter).

In vitro adhesion assay

imLECs were seeded onto a coated 96-well plate (Corning Costar). On the day of the assay, imLEC monolayers were preblocked or not with blocking antibodies for 1 h followed by the addition of 10,000 labeled WT DCs or 1:1 ratios of differently labeled *Tln1*^{-/-}:WT or *Itgbl*^{-/-}:WT, with blocking antibody or isotype. After 20 min, nonadherent cells were removed. Cells were washed twice with PBS and lifted with trypsin, and the number of DCs was quantified by flow cytometry on a CytoFlex S (Beckman Coulter).

Adoptive transfer experiments

Typically, 1–1.5 million CMFDA- or DR-labeled LPS mature DCs (ratio 1:1) were injected in INF or CTR mouse ears or footpads. Auricular and popliteal LNs were harvested at different time points, passaged through a 40- μm cell strainer and stained with BV421 rat anti-mouse MHC-II (BioLegend) and Pe/Cy7 hamster anti-mouse CD11c (BioLegend). Cell suspensions were acquired on a CytoFlex S and the total number of migratory labeled (CMFDA or DR) DCs analyzed in FlowJo. For VCAM-1 blocking experiments in CHS inflammation, 0.5 mg of VCAM-1 blocking antibody was administered i.p. after oxazolone challenge and 8 h before the adoptive transfer. 24 h after challenge, 1:1 ratios of

LPS mature *tln1*^{-/-} and WT DCs were injected together with 25 μg VCAM-1 blocking antibody (6C7.1; Engelhardt et al., 1998) or rat IgG1 isotype control (BioXCell) in INF ears and footpads. For integrin $\alpha 4$ blocking experiments, 1:1 ratios of LPS mature *tln1*^{-/-} and WT DCs were coinjected with 10 μg integrin $\alpha 4$ blocking antibody (PS/2; Miyake et al., 1991; BioXCell) or rat IgG2b isotype control (BioXCell) in either INF ears or footpads. 14 h (footpads) and 17 h (ear skin) later, dLNs were harvested and processed as described above. The whole LN was acquired on a Cytoflex S, and the total number of migratory labeled (CMFDA or DR) DCs analyzed in FlowJo.

Tail LECs isolation

Isolation and culturing protocols were adapted from Frye et al. (2018). Briefly, murine primary dermal LECs were isolated from the tail dermis of 4–6-wk-old littermate Cre⁺ (*Prox1-Cre*^{ERT2} *VCAM1*^{fl/fl}) or Cre⁻ control mice (WT or *VCAM1*^{fl/fl}) injected with tamoxifen (Sigma-Aldrich) as previously described. Tails were cut at the base and transferred in HBSS (Invitrogen) supplemented with 1% Pen/Strep (Invitrogen). The skin was removed from the tail and cut into 30-mm-long skin fragments, which were digested in 1.1 U/ml Dispase II (Roche) for 60 min at 37°C with agitation to separate the epidermis from the dermis. After a HBSS 1% Pen/Strep wash, the dermal fragments were digested for 90 min in a filter-sterilized solution of 1 mg/ml collagenase A (Roche) and 1.25 mM CaCl₂ (Sigma-Aldrich) under gentle agitation conditions. The digested fragments were filtered through a 70- μm cell strainer and seeded on 0.5% gelatin-coated cell culture plates in DMEM (Sigma-Aldrich), supplemented with Bovine Brain Extract (Lonza), 10% FBS, 50 $\mu\text{g/ml}$ heparin (PromoCell), 1% non-essential amino acids (Gibco), 1% Pen/Strep, and 1% glutamine (Thermo Fisher Scientific). After reaching confluency, cells were detached using Accutase detachment and were incubated for 45 min with dynabeads (Cellutron Life Technologies,) coupled to a-CD31 antibody (BD PharMingen; Cat, Clone MEC13.3). Dynabead-coupled cells were washed with 0.2% BSA in PBS and subcultured. The above-mentioned CD31 purification step was repeated once more, after which cells were passaged 1:3. Purity of cells was checked by FACS after this stage. The culturing conditions were a humidified incubator at 37°C, 5% CO₂. To analyze VCAM-1 expression, cells were stained with BV421 rat anti-mouse CD31, PE-Cy7 rat anti-mouse podoplanin, and AF647 rat anti-mouse VCAM-1 (Biolegend), and cells were acquired on a Cytoflex S and analyzed in FlowJo.

TPA-induced ear skin inflammation

Ears of mice were treated by applying topically 2 μg TPA (Sigma-Aldrich) dissolved in 20 μl acetone (10 μl on each side of the ear). 24 h later, ear thickness was measured with a caliper (Brütsch Rüeegg), and animals were used in FITC painting experiments or sacrificed to determine VCAM-1 expression in ECs present in inflamed ears.

FITC painting

Ears of mice were inflamed by topical application of TPA. 24 h later, FITC (5 mg/ml; Sigma-Aldrich) was dissolved in acetone

and dibutyl phthalate (1:1; Sigma-Aldrich), and 20 μ l was applied to each side of the ear. 18 h later, ear-draining auricular LNs were harvested and processed as described above. Cell suspensions were stained with PE/Cy7 Armenian hamster anti-mouse CD11c and BV421 rat anti-mouse MHC-II (both from BioLegend). For each sample, a total of 2×10^6 cells was acquired on a Cytotoflex S, and the percentage and number of FITC⁺ and FITC⁻ migratory cells were analyzed in FlowJo.

Statistical analyses

Statistical analyses and data representation were performed using GraphPad Prism 8 software (GraphPad). Normal distribution was assessed by applying the Shapiro-Wilk normality test. Depending on the outcome, two-tailed unpaired or paired (line-connected dots in graphs) Student's *t* test or unpaired Mann-Whitney test was used for simple comparisons. For multiple comparisons, unpaired one-way ANOVA followed by Tukey post hoc test or paired one-way ANOVA with the Geisser-Greenhouse correction were used. Unless otherwise indicated, data in graphs show mean \pm SEM. P values indicate the following significances: *, $P < 0.05$; **, $P < 0.01$; ***, $P < 0.001$; and ****, $P < 0.0001$.

Online supplemental material

Fig. S1 shows the characterization of dermal lymphatic capillaries and collectors. **Fig. S2** details the sequencing results of capLECs, colLECs, and BECs derived from CTR and INF skin. **Fig. S3** shows the expression of trafficking molecules in murine ear skin explants. **Fig. S4** characterizes that DC adhesion, transmigration, and crawling on lymphatic endothelial monolayers is integrin $\alpha 4\beta 1$ /VCAM-1 dependent. **Fig. S5** provides a characterization of the VCAM-1 knockdown efficiency achieved in *Prox1-Cre^{ERT2} Vcam1^{fl/fl}* mice. **Video 1** shows DCs entering into lymphatic capillaries in ear skin explants. **Video 2** provides a collection of videos showing DCs entering into lymphatic vessels with collector-like morphology in ear skin explants from *Prox-1 mOrange2* mice. **Video 3** provides a collection of videos showing DCs entering into lymphatic collectors in ear skin explants from WT mice costained for CD31 and LYVE-1 or *Prox-1 mOrange2* mice stained for LYVE-1. **Video 4** shows a DC entering into lymphatic collector in vivo. **Video 5** and **Video 6** represent whole-mount Z-stack animations showing fibrillar collagen in (**Video 5**) uninfamed and (**Video 6**) INF murine ear skin.

Acknowledgments

The authors thank Angela Vallone, Simone Haener, Simone Fenk, and the ETH Scientific Center for Optical and Electron Microscopy (ScopeM) for excellent technical assistance, and the staff of the ETH Rodent Center HCI for animal husbandry. Moreover, we thank Dietmar Vestweber (Max Planck Institute Münster, Münster, Germany) and Lothar Dieterich (ETH Zurich) for providing anti-VCAM-1 blocking antibody (6C7.1).

F. Kiefer was supported by the Deutsche Forschungsgemeinschaft (German Research Foundation; grants SFB1348/1-386797833 and SFB1450/1-431460824). C. Halin gratefully acknowledges financial

support from the Swiss National Science Foundation (grants 310030_182528 and 310030_156269) and from ETH Zurich.

Author contributions: J. Arasa and V. Collado-Diaz designed and performed experiments, analyzed and discussed data, and wrote the manuscript. I. Kritikos and J.D. Medina-Sanchez performed experiments, and analyzed and discussed data. M.C. Friess, E.C. Sigmund, P. Schineis, M.C. Hunter, and C. Tacconi performed experiments and analyzed data. N. Paterson, T. Lämmermann, and M. Moser provided $\beta 1$ - or talin-deficient bone marrow and discussed data. T. Nagasawa, F. Kiefer, T. Makinen, and M. Detmar provided mice or reagents and discussed data. C. Halin designed experiments, interpreted data, and wrote the manuscript.

Disclosures: The authors declare no competing interests exist.

Submitted: 3 July 2020

Revised: 22 February 2021

Accepted: 14 April 2021

References

- Akl, T.J., T. Nagai, G.L. Coté, and A.A. Gashev. 2011. Mesenteric lymph flow in adult and aged rats. *Am. J. Physiol. Heart Circ. Physiol.* 301:H1828-H1840. <https://doi.org/10.1152/ajpheart.00538.2011>
- Ara, T., K. Tokoyoda, T. Sugiyama, T. Egawa, K. Kawabata, and T. Nagasawa. 2003. Long-term hematopoietic stem cells require stromal cell-derived factor-1 for colonizing bone marrow during ontogeny. *Immunity*. 19: 257-267. [https://doi.org/10.1016/S1074-7613\(03\)00201-2](https://doi.org/10.1016/S1074-7613(03)00201-2)
- Baluk, P., J. Fuxe, H. Hashizume, T. Romano, E. Lashnits, S. Butz, D. Vestweber, M. Corada, C. Molendini, E. Dejana, and D.M. McDonald. 2007. Functionally specialized junctions between endothelial cells of lymphatic vessels. *J. Exp. Med.* 204:2349-2362. <https://doi.org/10.1084/jem.20062596>
- Bazigou, E., S. Xie, C. Chen, A. Weston, N. Miura, L. Sorokin, R. Adams, A.F. Muro, D. Sheppard, and T. Makinen. 2009. Integrin- $\alpha 9$ is required for fibronectin matrix assembly during lymphatic valve morphogenesis. *Dev. Cell*. 17:175-186. <https://doi.org/10.1016/j.devcel.2009.06.017>
- Berk, D.A., M.A. Swartz, A.J. Leu, and R.K. Jain. 1996. Transport in lymphatic capillaries. II. Microscopic velocity measurement with fluorescence photobleaching. *Am. J. Physiol.* 270:H330-H337. <https://doi.org/10.1152/ajpheart.1996.270.1.H330>
- Brinkman, C.C., D. Iwami, M.K. Hritzo, Y. Xiong, S. Ahmad, T. Simon, K.L. Hippen, B.R. Blazar, and J.S. Bromberg. 2016. Treg engage lymphotoxin beta receptor for afferent lymphatic transendothelial migration. *Nat. Commun.* 7:12021. <https://doi.org/10.1038/ncomms12021>
- Butler, G.S., R.A. Dean, E.M. Tam, and C.M. Overall. 2008. Pharmacoproteomics of a metalloproteinase hydroxamate inhibitor in breast cancer cells: dynamics of membrane type 1 matrix metalloproteinase-mediated membrane protein shedding. *Mol. Cell. Biol.* 28:4896-4914. <https://doi.org/10.1128/MCB.01775-07>
- Calderwood, D.A., and M.H. Ginsberg. 2003. Talin forges the links between integrins and actin. *Nat. Cell Biol.* 5:694-696. <https://doi.org/10.1038/ncb0803-694>
- Choi, I., H.K. Chung, S. Ramu, H.N. Lee, K.E. Kim, S. Lee, J. Yoo, D. Choi, Y.S. Lee, B. Aguilar, and Y.K. Hong. 2011. Visualization of lymphatic vessels by Prox1-promoter directed GFP reporter in a bacterial artificial chromosome-based transgenic mouse. *Blood*. 117:362-365. <https://doi.org/10.1182/blood-2010-07-298562>
- Christiansen, A.J., L.C. Dieterich, I. Ohs, S.B. Bachmann, R. Bianchi, S.T. Proulx, M. Hollmén, D. Aebischer, and M. Detmar. 2016. Lymphatic endothelial cells attenuate inflammation via suppression of dendritic cell maturation. *Oncotarget*. 7:39421-39435. <https://doi.org/10.18632/oncotarget.9820>
- Clausen, B.E., and P. Stoitzner. 2015. Functional Specialization of Skin Dendritic Cell Subsets in Regulating T Cell Responses. *Front. Immunol.* 6:534. <https://doi.org/10.3389/fimmu.2015.00534>

- de Boer, J., A. Williams, G. Skavdis, N. Harker, M. Coles, M. Tolaini, T. Norton, K. Williams, K. Roderick, A.J. Potocnik, and D. Kioussis. 2003. Transgenic mice with hematopoietic and lymphoid specific expression of Cre. *Eur. J. Immunol.* 33:314–325. <https://doi.org/10.1002/immu.200310005>
- Dixon, J.B., S.T. Greiner, A.A. Gashev, G.L. Cote, J.E. Moore, and D.C. Zawieja. 2006. Lymph flow, shear stress, and lymphocyte velocity in rat mesenteric prenodal lymphatics. *Microcirculation.* 13:597–610. <https://doi.org/10.1080/10739680600893909>
- Engelhardt, B., M. Laschinger, M. Schulz, U. Samulowitz, D. Vestweber, and G. Hoch. 1998. The development of experimental autoimmune encephalomyelitis in the mouse requires alpha4-integrin but not alpha4beta7-integrin. *J. Clin. Invest.* 102:2096–2105. <https://doi.org/10.1172/JCI4271>
- Förster, R., A. Schubel, D. Breitfeld, E. Kremmer, I. Renner-Müller, E. Wolf, and M. Lipp. 1999. CCR7 coordinates the primary immune response by establishing functional microenvironments in secondary lymphoid organs. *Cell.* 99:23–33. [https://doi.org/10.1016/S0092-8674\(00\)80059-8](https://doi.org/10.1016/S0092-8674(00)80059-8)
- Frye, M., A. Taddei, C. Dierkes, I. Martinez-Corral, M. Fielden, H. Ortsäter, J. Kazenwadel, D.P. Calado, P. Ostergaard, M. Salminen, et al. 2018. Matrix stiffness controls lymphatic vessel formation through regulation of a GATA2-dependent transcriptional program. *Nat. Commun.* 9:1511. <https://doi.org/10.1038/s41467-018-03959-6>
- Galili, T., A. O'Callaghan, J. Sidi, and C. Sievert. 2018. heatmaply: an R package for creating interactive cluster heatmaps for online publishing. *Bioinformatics.* 34:1600–1602. <https://doi.org/10.1093/bioinformatics/btx657>
- Garnier, L., A.O. Kountidi, and S. Hugues. 2019. Tumor-Associated Lymphatic Vessel Features and Immunomodulatory Functions. *Front. Immunol.* 10:720. <https://doi.org/10.3389/fimmu.2019.00720>
- Hägerling, R., C. Pollmann, L. Kremer, V. Andresen, and F. Kiefer. 2011. Intravital two-photon microscopy of lymphatic vessel development and function using a transgenic Prox1 promoter-directed mOrange2 reporter mouse. *Biochem. Soc. Trans.* 39:1674–1681. <https://doi.org/10.1042/BST20110722>
- Hunter, M.C., A. Teijeira, R. Montecchi, E. Russo, P. Runge, F. Kiefer, and C. Halin. 2019. Dendritic Cells and T Cells Interact Within Murine Afferent Lymphatic Capillaries. *Front. Immunol.* 10:520. <https://doi.org/10.3389/fimmu.2019.00520>
- Johnson, L.A., and D.G. Jackson. 2013. The chemokine CX3CL1 promotes trafficking of dendritic cells through inflamed lymphatics. *J. Cell Sci.* 126: 5259–5270. <https://doi.org/10.1242/jcs.135343>
- Johnson, L.A., S. Clasper, A.P. Holt, P.F. Lalor, D. Baban, and D.G. Jackson. 2006. An inflammation-induced mechanism for leukocyte transmigration across lymphatic vessel endothelium. *J. Exp. Med.* 203: 2763–2777. <https://doi.org/10.1084/jem.20051759>
- Kabashima, K., N. Shiraishi, K. Sugita, T. Mori, A. Onoue, M. Kobayashi, J. Sakabe, R. Yoshiki, H. Tamamura, N. Fujii, et al. 2007. CXCL12-CXCR4 engagement is required for migration of cutaneous dendritic cells. *Am. J. Pathol.* 171:1249–1257. <https://doi.org/10.2353/ajpath.2007.070225>
- Kissenpfennig, A., S. Henri, B. Dubois, C. Laplace-Builhé, P. Perrin, N. Romani, C.H. Tripp, P. Douillard, L. Leserman, D. Kaiserlian, et al. 2005. Dynamics and function of Langerhans cells in vivo: dermal dendritic cells colonize lymph node areas distinct from slower migrating Langerhans cells. *Immunity.* 22:643–654. <https://doi.org/10.1016/j.immuni.2005.04.004>
- Koni, P.A., S.K. Joshi, U.A. Temann, D. Olson, L. Burkly, and R.A. Flavell. 2001. Conditional vascular cell adhesion molecule 1 deletion in mice: impaired lymphocyte migration to bone marrow. *J. Exp. Med.* 193:741–754. <https://doi.org/10.1084/jem.193.6.741>
- Kühn, R., F. Schwenk, M. Aguet, and K. Rajewsky. 1995. Inducible gene targeting in mice. *Science.* 269:1427–1429. <https://doi.org/10.1126/science.7660125>
- Lämmermann, T., B.L. Bader, S.J. Monkley, T. Worbs, R. Wedlich-Söldner, K. Hirsch, M. Keller, R. Förster, D.R. Critchley, R. Fässler, and M. Sixt. 2008. Rapid leukocyte migration by integrin-independent flowing and squeezing. *Nature.* 453:51–55. <https://doi.org/10.1038/nature06887>
- Lappin, M.B., J.M. Weiss, V. Delattre, B. Mai, H. Dittmar, C. Maier, K. Manke, S. Grabbe, S. Martin, and J.C. Simon. 1999. Analysis of mouse dendritic cell migration in vivo upon subcutaneous and intravenous injection. *Immunology.* 98:181–188. <https://doi.org/10.1046/j.1365-2567.1999.00850.x>
- Lindquist, R.L., G. Shakhbar, D. Dudziak, H. Wardemann, T. Eisenreich, M.L. Dustin, and M.C. Nussenzweig. 2004. Visualizing dendritic cell networks in vivo. *Nat. Immunol.* 5:1243–1250. <https://doi.org/10.1038/nri139>
- Lutz, M.B., N. Kukutsch, A.L. Ogilvie, S. Rössner, F. Koch, N. Romani, and G. Schuler. 1999. An advanced culture method for generating large quantities of highly pure dendritic cells from mouse bone marrow. *J. Immunol. Methods.* 223:77–92. [https://doi.org/10.1016/S0022-1759\(98\)00204-X](https://doi.org/10.1016/S0022-1759(98)00204-X)
- Mäkinen, T., R.H. Adams, J. Bailey, Q. Lu, A. Ziemiecki, K. Alitalo, R. Klein, and G.A. Wilkinson. 2005. PDZ interaction site in ephrinB2 is required for the remodeling of lymphatic vasculature. *Genes Dev.* 19:397–410. <https://doi.org/10.1101/gad.330105>
- Martín-Fontecha, A., S. Sebastiani, U.E. Höpken, M. Uguccioni, M. Lipp, A. Lanzavecchia, and F. Sallusto. 2003. Regulation of dendritic cell migration to the draining lymph node: impact on T lymphocyte traffic and priming. *J. Exp. Med.* 198:615–621. <https://doi.org/10.1084/jem.20030448>
- Miyake, K., I.L. Weissman, J.S. Greenberger, and P.W. Kincade. 1991. Evidence for a role of the integrin VLA-4 in lympho-hemopoiesis. *J. Exp. Med.* 173:599–607. <https://doi.org/10.1084/jem.173.3.599>
- Moore, J.E. Jr., and C.D. Bertram. 2018. Lymphatic System Flows. *Annu. Rev. Fluid Mech.* 50:459–482. <https://doi.org/10.1146/annurev-fluid-122316-045259>
- Nitschké, M., D. Aebischer, M. Abadier, S. Haener, M. Lucic, B. Vigl, H. Luche, H.J. Fehling, O. Biehlaier, R. Lyck, and C. Halin. 2012. Differential requirement for ROCK in dendritic cell migration within lymphatic capillaries in steady-state and inflammation. *Blood.* 120:2249–2258. <https://doi.org/10.1182/blood-2012-03-417923>
- Nourshargh, S., P.L. Hordijk, and M. Sixt. 2010. Breaching multiple barriers: leukocyte motility through venular walls and the interstitium. *Nat. Rev. Mol. Cell Biol.* 11:366–378. <https://doi.org/10.1038/nrm2889>
- Ohl, L., M. Mohaupt, N. Czeloth, G. Hintzen, Z. Kiafard, J. Zwirner, T. Blankenstein, G. Henning, and R. Förster. 2004. CCR7 governs skin dendritic cell migration under inflammatory and steady-state conditions. *Immunity.* 21:279–288. <https://doi.org/10.1016/j.immuni.2004.06.014>
- Petrich, B.G., P. Marchese, Z.M. Ruggeri, S. Spiess, R.A. Weichert, F. Ye, R. Tiedt, R.C. Skoda, S.J. Monkley, D.R. Critchley, and M.H. Ginsberg. 2007. Talin is required for integrin-mediated platelet function in hemostasis and thrombosis. *J. Exp. Med.* 204:3103–3111. <https://doi.org/10.1084/jem.20071800>
- Petrova, T.V., and G.Y. Koh. 2018. Organ-specific lymphatic vasculature: From development to pathophysiology. *J. Exp. Med.* 215:35–49. <https://doi.org/10.1084/jem.20171868>
- Pflicke, H., and M. Sixt. 2009. Preformed portals facilitate dendritic cell entry into afferent lymphatic vessels. *J. Exp. Med.* 206:2925–2935. <https://doi.org/10.1084/jem.20091739>
- Podgrabska, S., O. Kamalu, L. Mayer, M. Shimaoka, H. Snoeck, G.J. Randolph, and M. Skobe. 2009. Inflamed lymphatic endothelium suppresses dendritic cell maturation and function via Mac-1/ICAM-1-dependent mechanism. *J. Immunol.* 183:1767–1779. <https://doi.org/10.4049/jimmunol.0802167>
- Potocnik, A.J., C. Brakebusch, and R. Fässler. 2000. Fetal and adult hematopoietic stem cells require beta1 integrin function for colonizing fetal liver, spleen, and bone marrow. *Immunity.* 12:653–663. [https://doi.org/10.1016/S1074-7613\(00\)80216-2](https://doi.org/10.1016/S1074-7613(00)80216-2)
- Ratzinger, G., P. Stoitzner, S. Ebner, M.B. Lutz, G.T. Layton, C. Rainer, R.M. Senior, J.M. Shipley, P. Fritsch, G. Schuler, and N. Romani. 2002. Matrix metalloproteinases 9 and 2 are necessary for the migration of Langerhans cells and dermal dendritic cells from human and murine skin. *J. Immunol.* 168:4361–4371. <https://doi.org/10.4049/jimmunol.168.9.4361>
- Reynolds, G., P. Vegh, J. Fletcher, E.F.M. Poyner, E. Stephenson, I. Goh, R.A. Botting, N. Huang, B. Olabi, A. Dubois, et al. 2021. Developmental cell programs are co-opted in inflammatory skin disease. *Science.* 371: eaba6500. <https://doi.org/10.1126/science.aba6500>
- Russo, E., A. Teijeira, K. Vaahhtomeri, A.H. Willrodt, J.S. Bloch, M. Nitschké, L. Santambrogio, D. Kerjaschki, M. Sixt, and C. Halin. 2016. Intra-lymphatic CCL21 Promotes Tissue Egress of Dendritic Cells through Afferent Lymphatic Vessels. *Cell Rep.* 14:1723–1734. <https://doi.org/10.1016/j.celrep.2016.01.048>
- Schneis, P., P. Runge, and C. Halin. 2019. Cellular traffic through afferent lymphatic vessels. *Vascul. Pharmacol.* 112:31–41. <https://doi.org/10.1016/j.vph.2018.08.001>
- Swartz, M.A., D.A. Berk, and R.K. Jain. 1996. Transport in lymphatic capillaries. I. Macroscopic measurements using residence time distribution theory. *Am. J. Physiol.* 270:H324–H329. <https://doi.org/10.1152/ajpheart.1996.270.1.H324>

- Tal, O., H.Y. Lim, I. Gurevich, I. Milo, Z. Shipony, L.G. Ng, V. Angeli, and G. Shakhar. 2011. DC mobilization from the skin requires docking to immobilized CCL21 on lymphatic endothelium and intralymphatic crawling. *J. Exp. Med.* 208:2141–2153. <https://doi.org/10.1084/jem.20102392>
- Teijeira, A., S. Garasa, R. Peláez, A. Azpilikueta, C. Ochoa, D. Marré, M. Rodrigues, C. Alfaro, C. Aubá, S. Valitutti, et al. 2013. Lymphatic endothelium forms integrin-engaging 3D structures during DC transit across inflamed lymphatic vessels. *J. Invest. Dermatol.* 133:2276–2285. <https://doi.org/10.1038/jid.2013.152>
- Teijeira, A., M.C. Hunter, E. Russo, S.T. Proulx, T. Frei, G.F. Debes, M. Coles, I. Melero, M. Detmar, A. Rouzaut, and C. Halin. 2017. T Cell Migration from Inflamed Skin to Draining Lymph Nodes Requires Intralymphatic Crawling Supported by ICAM-1/LFA-1 Interactions. *Cell Rep.* 18: 857–865. <https://doi.org/10.1016/j.celrep.2016.12.078>
- Teoh, D., L.A. Johnson, T. Hanke, A.J. McMichael, and D.G. Jackson. 2009. Blocking development of a CD8+ T cell response by targeting lymphatic recruitment of APC. *J. Immunol.* 182:2425–2431. <https://doi.org/10.4049/jimmunol.0803661>
- Tomura, M., A. Hata, S. Matsuoka, F.H. Shand, Y. Nakanishi, R. Ikebuchi, S. Ueha, H. Tsutsui, K. Inaba, K. Matsushima, et al. 2014. Tracking and quantification of dendritic cell migration and antigen trafficking between the skin and lymph nodes. *Sci. Rep.* 4:6030. <https://doi.org/10.1038/srep06030>
- Ulvmar, M.H., and T. Mäkinen. 2016. Heterogeneity in the lymphatic vascular system and its origin. *Cardiovasc. Res.* 111:310–321. <https://doi.org/10.1093/cvr/cvw175>
- Vigl, B., D. Aebischer, M. Nitschké, M. Iolyeva, T. Röthlin, O. Antsiferova, and C. Halin. 2011. Tissue inflammation modulates gene expression of lymphatic endothelial cells and dendritic cell migration in a stimulus-dependent manner. *Blood.* 118:205–215. <https://doi.org/10.1182/blood-2010-12-326447>
- Wang, X.N., N. McGovern, M. Gunawan, C. Richardson, M. Windebank, T.W. Siah, H.Y. Lim, K. Fink, J.L. Yao Li, L.G. Ng, et al. 2014. A three-dimensional atlas of human dermal leukocytes, lymphatics, and blood vessels. *J. Invest. Dermatol.* 134:965–974. <https://doi.org/10.1038/jid.2013.481>
- Weber, M., R. Hauschild, J. Schwarz, C. Moussion, I. de Vries, D.F. Legler, S.A. Luther, T. Bollenbach, and M. Sixt. 2013. Interstitial dendritic cell guidance by haptotactic chemokine gradients. *Science.* 339:328–332. <https://doi.org/10.1126/science.1228456>
- Worbs, T., S.I. Hammerschmidt, and R. Förster. 2017. Dendritic cell migration in health and disease. *Nat. Rev. Immunol.* 17:30–48. <https://doi.org/10.1038/nri.2016.116>
- Zal, T., A. Volkman, and B. Stockinger. 1994. Mechanisms of tolerance induction in major histocompatibility complex class II-restricted T cells specific for a blood-borne self-antigen. *J. Exp. Med.* 180:2089–2099. <https://doi.org/10.1084/jem.180.6.2089>

Supplemental material

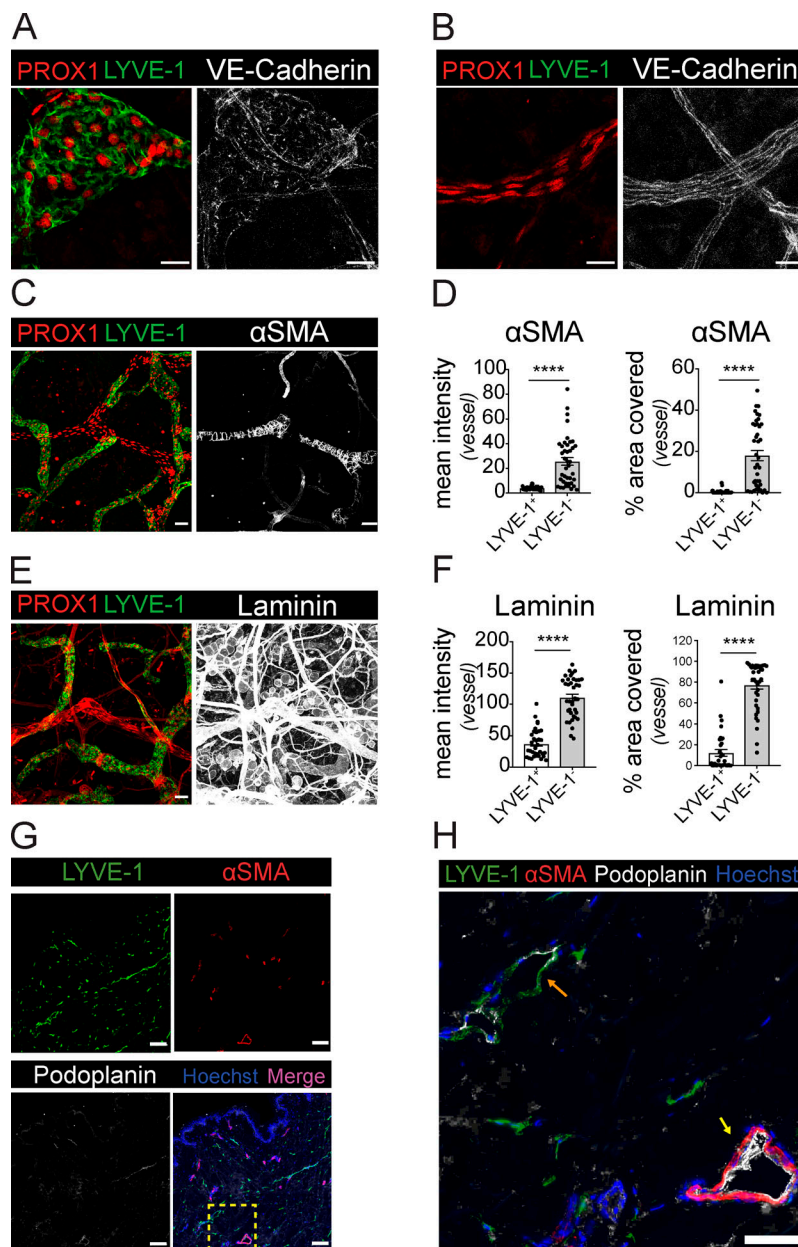


Figure S1. **Characterization of dermal lymphatic LYVE-1⁺ capillaries and LYVE-1⁻ collectors.** (A–F) Mouse ear skin whole-mounts were analyzed by immunofluorescence to validate the suitability of LYVE-1 as a marker for differentiating between lymphatic capillaries and collectors. In contrast to dermal lymphatic LYVE-1⁻ collectors, dermal lymphatic LYVE-1⁺ capillaries are characterized by VE-cadherin⁺ button-like cell–cell junctions (A and B), the absence of smooth muscle cell coverage (C and D), and a thin BM (E and F). Scale bars in A–C and E, 50 μ m. Representative images from three to five experiments are shown. Quantifications of α SMA (D) and laminin (n = pooled whole-mount data from 3–5 mice per condition; G). (G and H) Presence of α SMA-covered collectors in human skin. Immunofluorescence staining for α SMA, podoplanin (podo), LYVE-1, and Hoechst was performed in healthy human skin. The yellow box in G highlights the enlarged region shown in H. Orange arrow, podo⁺ LYVE-1⁺ α SMA⁻ capillary; yellow arrow, podo⁺ LYVE-1⁻ α SMA⁺ collector. Scale bars, 100 μ m (overview) and 50 μ m (zoomed-in image). Images obtained in one out of three different skin biopsies analyzed are shown. (D and F) Unpaired Mann–Whitney test. ****, $P < 0.0001$.

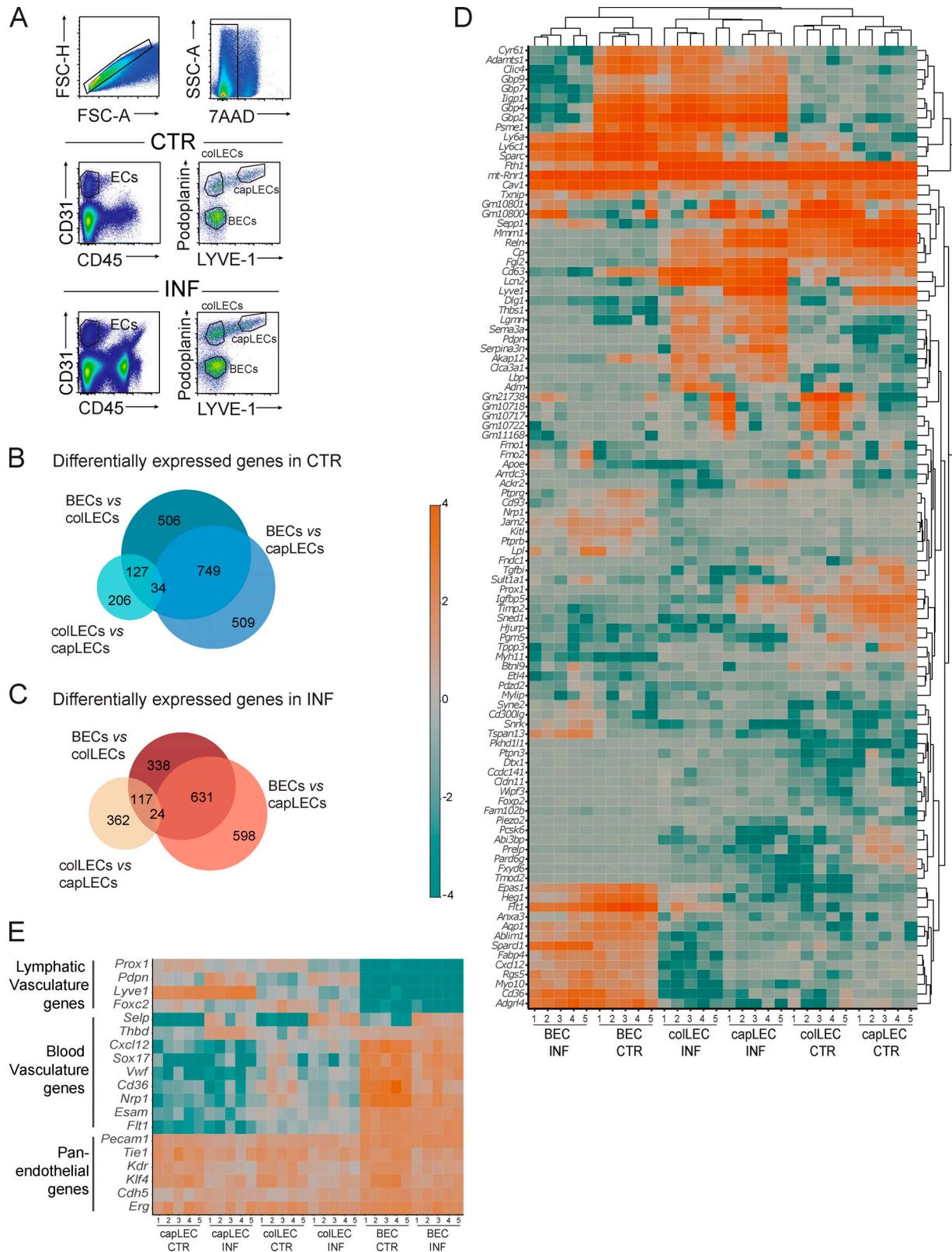


Figure S2. **Sequencing results of capLECs, colLECs, and BECs derived from control and CHS-inflamed skin.** (A) Gating strategy used for FACS sorting of singlet, 7AAD⁻ capLECs (CD45⁻CD31⁺podo⁺LYVE-1⁺), colLECs (CD45⁻CD31⁺podo⁺LYVE-1⁻), and BECs (CD45⁻CD31⁺podo⁻LYVE-1⁻). (B and C) Euler diagrams showing number of differentially expressed genes (0.5-fold; P value, 0.05) in BECs versus colLECs/BECs versus capLECs/colLECs versus capLECs in CTR skin (B) and in INF skin (C). (D) Sample clustering of capLECs, colLECs, and BECs from INF and CTR mice showing the top 100 most variable genes. (E) Heatmap showing lymphatic, blood, and pan-endothelial genes in capLECs, colLECs, and BECs from INF and CTR mice (n = 5 experimental replicates). FSC-A, forward scatter area; FSC-H, forward scatter height; podo, podoplanin; SSC-A, side scatter area.

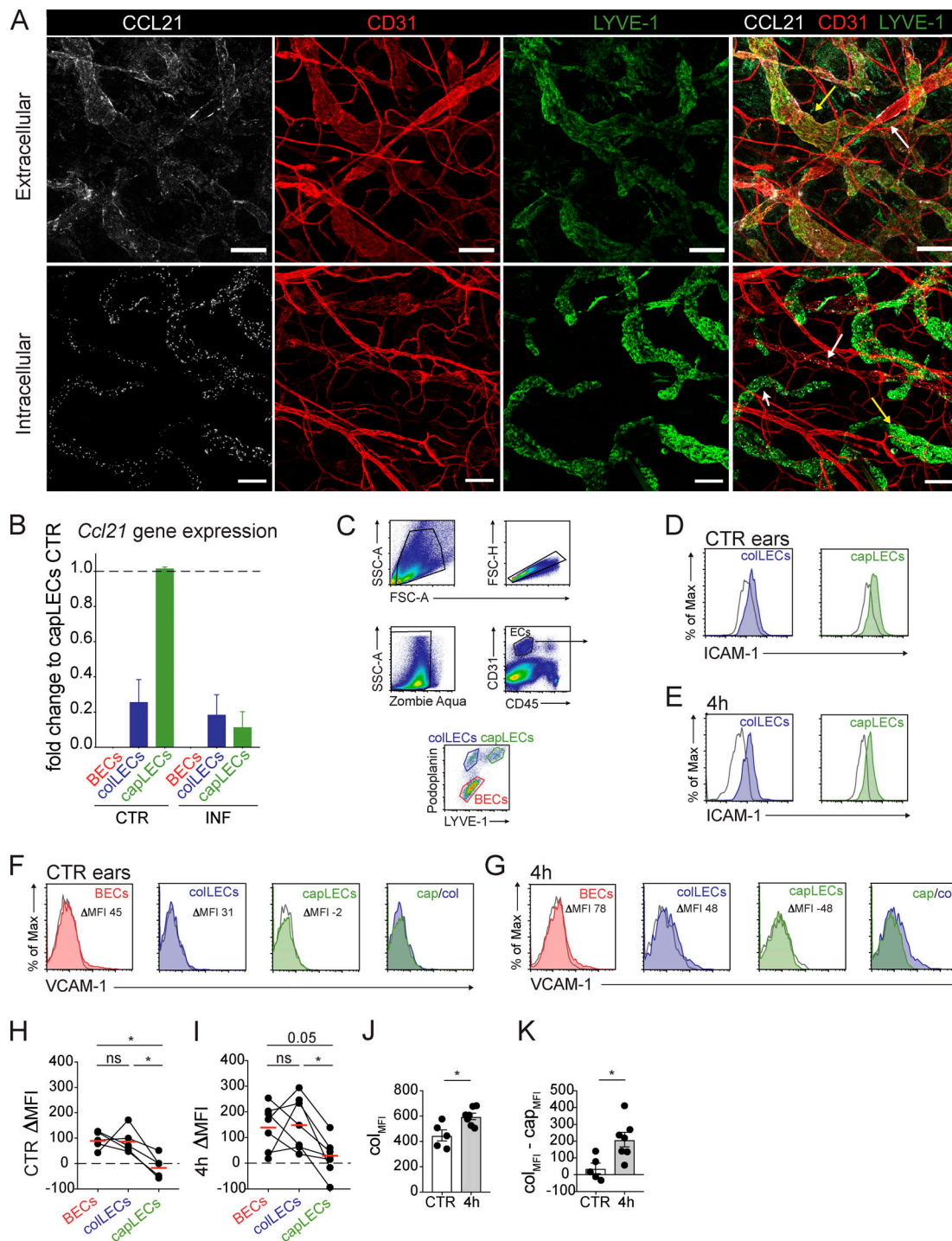


Figure S3. **Analysis of CCL21 in murine ear skin and of ICAM-1, VCAM-1, laminin, and fibrillar collagen expression in ear skin explants. (A)** Representative whole-mount picture of uninflamed murine ear skin showing intracellular and extracellular CCL21 protein levels (white) in CD31⁺ (red) LYVE-1⁺ (green) capillaries and CD31⁺LYVE-1⁻ collectors. Scale bar, 100 μ m. **(B)** Quantitative PCR analysis of *Ccl21* was performed on RNA isolated from FACS-sorted endothelial cells derived from CTR and INF murine ear skin. The same gating scheme as in Fig. S2 A was used for cell isolation ($n = 3$ experiments; two mice per condition were pooled). **(C–K)** FACS analysis of ICAM-1 and VCAM-1 expression in single-cell suspensions of freshly isolated CTR ear skin or upon ear skin incubation for 4 h in medium. **(C)** Depiction of the gating scheme used to identify singlet, live (ZombieAqua⁻) capLECs (CD45⁻ CD31⁺ podo⁺ LYVE-1⁺), colLECs (CD45⁻ CD31⁺ podo⁺ LYVE-1⁻), and BECs (CD45⁻ CD31⁺ podo⁻ LYVE-1⁻). **(D and E)** Representative FACS plots of ICAM-1 expression (shaded histogram) at 0 h (CTR; D) or after 4 h (E) of incubation. **(F and G)** Representative FACS plots of VCAM-1 expression at 0 h (CTR; F) and after 4 h (G) of incubation. Shaded histogram, VCAM-1; empty histogram, isotype control. **(H and I)** Quantification of the delta median fluorescent intensities (Δ MFI; specific-isotype staining) of the experiments performed in F and G. Measurements deriving from the same explant are connected by a line. **(J)** Summary of MFIs measured for colLECs at time 0 (CTR) and after 4 h of incubation. **(K)** Summary of the Δ MFIs measured per experiment between colLECs and capLECs. Each dot represents the value from one experiment. **(H and I)** Paired one-way ANOVA with the Geisser–Greenhouse correction. **(J and K)** unpaired Student's *t* test. *, $P < 0.05$. cap, capillaries; col, collectors; FSC-A, forward scatter area; FSC-H, forward scatter height; Max, maximum; podo, podoplanin; SSC-A, side scatter area.

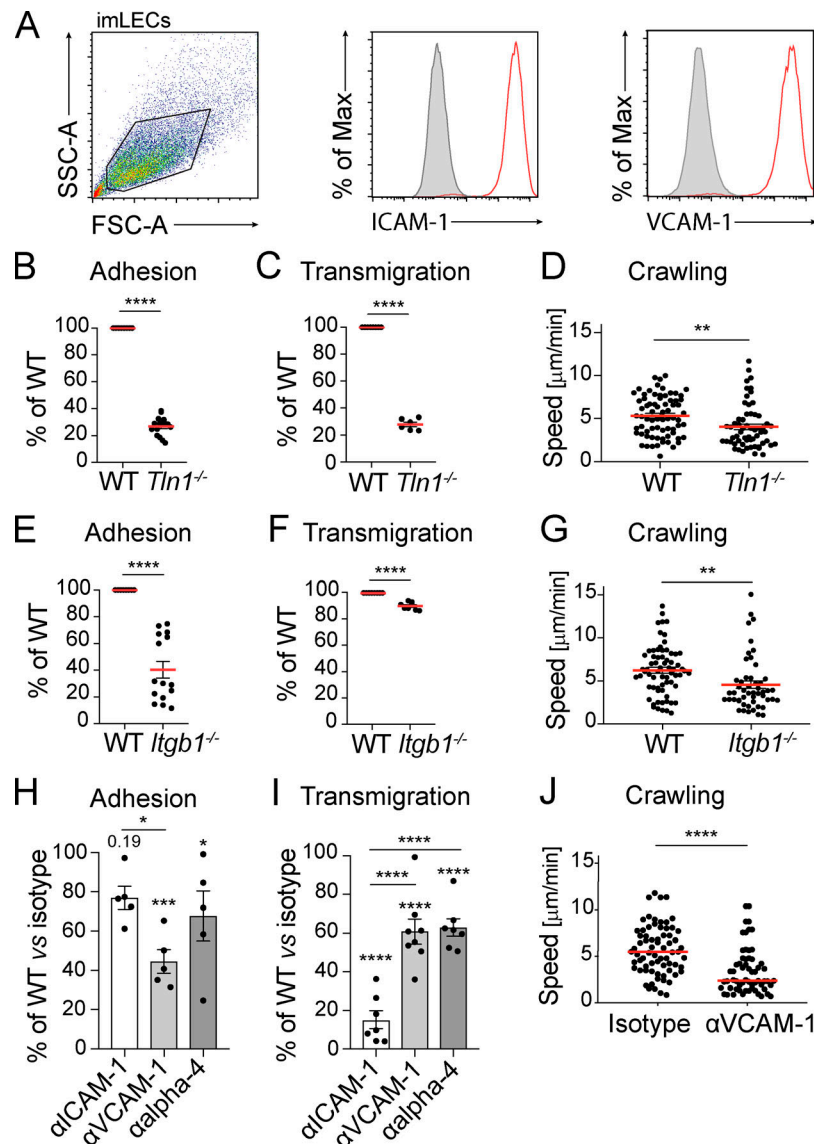


Figure S4. DC adhesion, transmigration, and crawling on lymphatic endothelial monolayers is integrin $\alpha4\beta1$ /VCAM-1 dependent. In vitro functional assays were performed on inflamed imLEC monolayers. **(A–C)** Representative FACS plots of imLECs showing ICAM-1 and VCAM-1 expression (red lines) in comparison to isotype control (gray shading). Analysis of adhesion **(B)** and transmigration **(C)** of *Tln1*^{-/-} DCs as compared with WT DCs. **(D)** Analysis of the speed of *Tln1*^{-/-} and WT DCs. Analysis of adhesion **(E)** and transmigration **(F)** of *Itgb1*^{-/-} DCs as compared with WT DCs. **(G)** Analysis of the speed of *Itgb1*^{-/-} and WT DCs. Analysis of adhesion **(H)** and transmigration **(I)** of WT DCs after treatment with 10 μ g/ml anti-ICAM-1, 25 μ g/ml anti-VCAM-1, or 10 μ g/ml anti-integrin $\alpha4$ as compared with treatment with the corresponding isotype control. **(B, C, E, F, H, and I)** Pooled data from three independent experiments are shown. **(J)** Speed of WT DCs in the presence of 25 μ g/ml anti-VCAM-1 or isotype control. **(D, G, and J)** One representative out of three similar experiments is shown. Each dot represents a single cell. Red line represents the mean. **(B–G and J)** Unpaired Student's *t* test. **(H and I)** Unpaired one-way ANOVA followed by Tukey post hoc test. *, *P* < 0.05; **, *P* < 0.01; ***, *P* < 0.001; and ****, *P* < 0.0001. FSC-A, forward scatter area; Max, maximum; SSC-A, side scatter area.

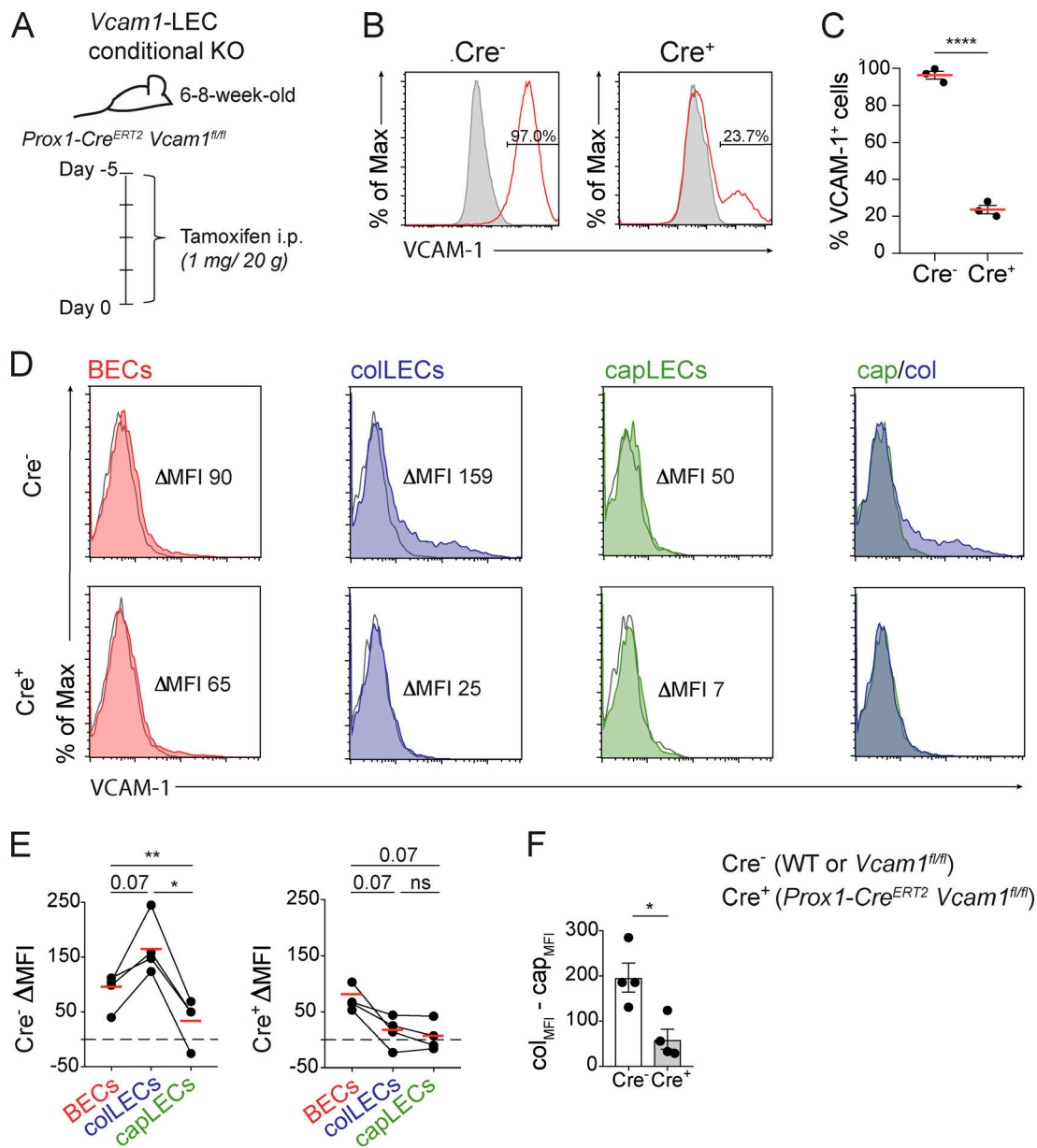


Figure S5. Confirmation of the LEC-specific loss of VCAM-1 in *Prox1-Cre^{ERT2} Vcam1^{fl/fl}* mice. (A) LEC-specific deletion of VCAM-1 was induced in *Prox1-Cre^{ERT2} Vcam1^{fl/fl}* mice by i.p. administration of tamoxifen. (B and C) Deletion of VCAM-1 was confirmed by analyzing VCAM-1 expression in IFN γ - and TNF α -stimulated primary LECs isolated from tail skin of tamoxifen-treated *Cre⁺ (Prox1-Cre^{ERT2} Vcam1^{fl/fl})* or *Cre⁻* control mice (WT or *Vcam1^{fl/fl}*). Representative FACS plots with respective percentages of VCAM-1⁺ cells are shown in B. Isotype control is shown as a gray shaded histogram. Quantification of percentage of VCAM-1⁺ cells is presented in C. Data from three experiments are shown. (D and E) FACS-based analysis of VCAM-1 expression in endothelial cells present in TPA-inflamed ear skin of *Cre⁺* or *Cre⁻* control mice. Shaded histogram: VCAM-1. Empty histogram: Isotype control. (D) Representative FACS plots. (E) Summary of the delta median fluorescent intensities (Δ MFI: specific-isotype staining) from all experiments performed ($n = 4$ mice per genotype). Measurements from the same mouse are connected by a line. (G) Summary of the Δ MFI measured per experiment between colLECs and capLECs. (C and F) Unpaired Student's *t* test. (E) Paired one-way ANOVA with the Geisser–Greenhouse correction. *, $P < 0.05$; **, $P < 0.01$; and ****, $P < 0.0001$. cap, capillaries; col, collectors; Max, maximum.

Video 1. Video showing DCs entering into lymphatic capillaries in ear skin explants. Crawl-in experiments with DeepRed labeled bone marrow-derived DCs (white) were performed in explants from *Prox1-mOrange2* (red) mice stained for LYVE-1 (green). After 1 h of incubation, DCs could be observed inside and entering into lymphatic capillaries. Videos were generated from three-dimensional reconstructions of Z-stacks. Video specifications: 30-s intervals, 10 frames/s (300 \times accelerated). Original length of the video: 30–90 min. Scale bar, 100 μ m. Video length: 38 s.

Video 2. Collection of videos from three independent experiments showing DCs entering into lymphatic collectors in ear skin explants. Experiments 1 and 2: Crawl-in experiments with CMFDA- or DeepRed-labeled bone marrow-derived DCs (white). Experiment 3: Crawl-in experiment with eYFP + DCs (green). All three experiments were performed in explants from *Prox1-mOrange2* (red) mice. After 2–4 h of incubation, DCs (indicated by yellow arrows) could be observed entering into lymphatic vessels with collector-like morphology. Videos were generated from three-dimensional reconstructions of Z-stacks. Video specifications: 30-s intervals, 10 frames/s (300× accelerated). Original length of the video: 30–90 min. Scale bar, 100 μm. eYFP, enhanced YFP. Video length: 3 min 11 s.

Video 3. Collection of videos from five independent experiments showing DCs entering into lymphatic collectors in ear skin explants. Experiments 1–5: Crawl-in experiments with DeepRed-labeled bone marrow-derived DCs (white) were performed in explants from WT mice costained for CD31 (red) and LYVE-1 (green), or from *Prox1-mOrange2* (red) mice stained for LYVE-1 (green). After 2–4 h of incubation, DCs (indicated by yellow arrows) could be observed entering into LYVE-1⁺ lymphatic collectors. Videos were generated from three-dimensional reconstructions of Z-stacks. Video specifications: 30-s intervals, 10 frames/s (300× accelerated). Original length of the video: 30–90 min. Scale bar, 100 μm. Video length: 3 min 16 s.

Video 4. Video showing a DC entry into lymphatic collector in vivo. IVM was performed on INF ear skin of anesthetized *Prox1-mOrange YFP-CD11c* mouse. The yellow arrow indicates a DC (green) entering into a lymphatic collector (red) and being quickly flushed downstream. The video was generated from three-dimensional reconstructions of Z-stacks. Video specifications: 30-s intervals, 15 frames/s (450× accelerated). Original length of the video: 26.5 min. Scale bar, 100 μm. Video length: 13 s.

Video 5. Video of the collagen surrounding an uninfamed lymphatic collector. Representative whole-mount Z-stack animation of uninfamed murine ear skin showing fibrillar collagen (white; determined by SHG) surrounding a PROX1⁺ lymphatic collector (red). Video specifications: 10 stacks/s. Scale bar, 10 μm. Video length: 20 s.

Video 6. Video of the collagen surrounding an inflamed lymphatic collector. Representative whole-mount Z-stack animation of CHS-inflamed murine ear skin showing fibrillar collagen (white; determined by SHG) surrounding a PROX1⁺ lymphatic collector (red). Video specifications: 10 stacks/s. Scale bar, 10 μm. Video length: 9 s.